Energy 353 (2026) 140801

Contents lists available at ScienceDirect

Energy

journal homepage: www.elsevier.com/locate/energy

Numerical study of near-borehole coupled thermo-hydro-mechanical processes during stimulation of a synthetic geothermal reservoir

Wen Luo [a,b,*], Anne-Catherine Dieudonné [a], Josselin Ouf [a,b], Philip J. Vardon [a]

[a] Faculty of Civil Engineering and Geosciences, Delft University of Technology, Delft, 2628 CN, The Netherlands
[b] Department of Engineering Geology and Hydrogeology, RWTH Aachen, Aachen, D-52064, Germany

ARTICLE INFO

Keywords:
Geothermal energy
Soft stimulation
Thermo-hydro-mechanics
Fatigue damage

ABSTRACT

Soft stimulation technologies have been proposed as a means to reduce the breakdown pressure and mitigate the risk of induced seismicity during geothermal reservoir stimulation. Yet, the underlying mechanisms remain poorly understood due to the complexity of the coupled thermo-hydro-mechanical (THM) processes. In this work, a fully coupled THM model is developed to evaluate and compare the performance of different stimulation scenarios (monotonic, stepwise injection rate, cyclic injection rate or temperature, and stepwise combined with cyclic injection rate stimulation) on a synthetic, highly permeable reservoir with near-borehole clogging. Simulation results show that stepwise injection rate stimulation yields the most favourable outcomes, followed by the stepwise injection rate combined with cyclic injection rate stimulation. On the other hand, fatigue effects are seen to play a negligible role in the improved performance since the tensile stress at the fracture tip is relaxed with the continuous fracture growth. In addition, cyclic injection temperature stimulation is generally neither better nor worse than monotonic stimulation, but has slightly different characteristics, creating more local damage controlled by the period of the injection cycle. Cyclic injection rate stimulation can slightly reduce the peak pressure, compared with monotonic stimulation, but only when the injection rate is low. The reduction in peak pressure occurs due to the combination of thermally-induced stresses associated with cooling and incremental damage rather than any influence of fatigue. Stepwise or low-frequency cyclic injection rate stimulation are suggested rather than a high-frequency cyclic injection rate stimulation, while injection with cyclic temperatures is suggested when more local damage is wanted.

1. Introduction

Stimulation technologies are commonly performed operations to improve well performance in geo-energy reservoirs. However, conventional hydraulic stimulation has caused environmental concerns, especially the risk of induced seismicity. For example, the hydraulic stimulations performed in the Enhanced Geothermal System (EGS) project in Basel (Switzerland), in Strasbourg (France) and in Pohang (South Korea) were reported to induce felt earthquakes with magnitude of 3.4, 3.6 and 5.4 respectively, leading to the termination of the projects [1–3]. Alternatively, soft stimulation technology has been proposed to reduce the risk of induced seismicity while achieving the desired stimulation performance, since it requires lower pumping pressure. Several soft stimulation methods, including cyclic injection rate [4] and thermal stimulation [5], have been demonstrated to be effective, with different underlying mechanisms. Cyclic hydraulic stimulation requires alternating phases of high and low flow rates to induce fatigue damage. Its ability to lower the breakdown pressure has been demonstrated in laboratory experiments [6], mine-scale experiments [7] and field tests [4]. Thermal stimulation requires the injection of cold water to induce rock contraction, therefore thermally-induced stress, which could re-activate pre-existing fractures, and create new fractures at lower pumping pressure [5,8]. Successful thermal stimulation demonstrations include the test on Well H40 & H41 at the Los Humeros field in Mexico [5] and the test on HE-8 at Hellisheiði in Iceland [8].

Although successful implementations of cyclic and thermal stimulations have been reported, the underlying mechanisms remain poorly understood due to the complexity of the coupled thermo-hydro-mechanical (THM) processes including cyclic effects, illustrated in Fig. 1. During stimulation with cold water, the cooling effect can induce volumetric strain (shrinkage) in the rock mass which is restrained by surrounding media, leading to (tensile) thermal stresses. This thermal-to-mechanical effect, can induce new fractures or re-activate natural fractures. Conversely, the mechanical deformation may result in energy

* Corresponding author at: Faculty of Civil Engineering and Geosciences, Delft University of Technology, Delft, 2628 CN, The Netherlands.
E-mail address: W.Luo@tudelft.nl (W. Luo).

https://doi.org/10.1016/j.energy.2026.140801
Received 14 October 2025; Received in revised form 28 February 2026; Accepted 18 March 2026
Available online 23 March 2026

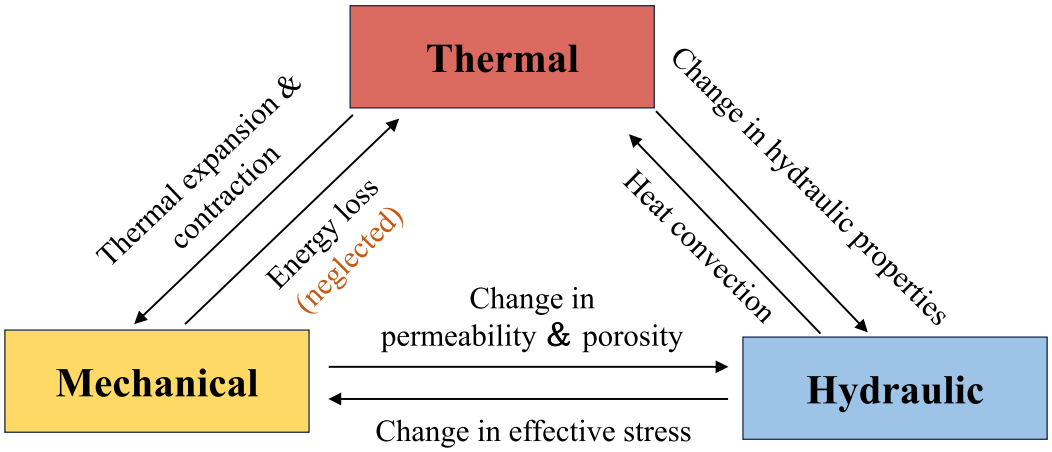

Fig. 1. Description of the interactions between thermo-hydro-mechanical (THM) processes.

loss, leading to changes in temperature. However, this mechanical-to-thermal effect is usually small and thus can be ignored in geomechanical analyses [9,10]. In addition, fluid properties such as viscosity and density [11] are influenced by temperature, and temperature changes may therefore induce or alter fluid flow. This thermal-to-hydraulic effect inevitably leads to injectivity decline during cold water injection. In contrast, any change in fluid pressure distribution induces a flow, which will influence heat transfer, thus the temperature field. This hydraulic-to-thermal effect largely controls the efficiency of heat extraction from the subsurface. Moreover, for the hydraulic-to-mechanical effect, rock deformation depends on the effective stress, which combines the total stress and pore pressure according to the effective stress principle [12]. On the other hand, deformation of the rock mass or the creation of new fluid pathways (i.e. new fractures or re-activated natural fractures) can change the fluid flow pattern. In addition, cyclic injection of stimulation fluid can reduce fluid and heat fluxes, compared to continuous injection, and cause cyclic pressure build-up and warming up, therefore resulting in cyclic changes in the stress field. Cyclic stress changes may lead to fatigue damage, or control fracture propagation, thus can largely influence the stimulation performance. For instance, a field test performed on well PX-1 at the Pohang EGS project site demonstrated that cyclic stimulation was able to improve injectivity from 0.5 L/(s MPa) to 2.6 L/(s MPa) while managing the seismic activity to remain below the target threshold of M_w 2.0 [4,13]. However, whether fatigue effect plays a dominant role in the injectivity or not, is yet clear. A thorough understanding of the coupled THM processes under cyclic stimulation is therefore of significant importance to understand the underlying mechanisms and to optimise the stimulation protocol.

Numerical simulation provides a possible way to investigate the underlying mechanisms and compare the stimulation performances under various stimulation strategies. Yoshioka et al. [14] used the GeoMechanical Reservoir Simulator to investigate the optimal design of water stimulation to a synthetic 3D reservoir, in which the fluid flow was allowed to happen in a single fracture plane. Yet, the model remained simple as the borehole was simplified as a line source and the matrix was assumed to be impermeable. In addition, the investigated stimulation scenarios were limited to continuous (followed by shut-in) and stepwise stimulation. Yoon et al. [15] used the Particle Flow Code^{2D} to study the optimised hydraulic stimulation of intact and naturally fractured reservoir. The investigated scenarios involved continuous and cyclic styles of pressure-controlled and flow rate-controlled injections. However, the cyclic frequency was low (cyclic period around 3 h) and the injection well was simplified as a point, thus ignoring the near-borehole effects. Jacquey et al. [16] constructed a 3D model with the hydraulic fracture being represented as boundary condition to simulate the cyclic hydraulic stimulation excercises performed in the well Gt GrSk 4/05 in GroßSchönebeck. Though the fracture opening was considered, this model was not able to simulate the fracture initiation and propagation and thermal effects are not included. Cheng et al. [17] generated a 3D stochastic fracture network model to simulate the phase 2.2 stimulation at the Newberry EGS site, with the fully THM processes considered. Yoo et al. [18] used TOUGH-FLAC simulator to simulate the hydraulic stimulation treatment to PX-1 and PX-2 in Pohang field, yet not included the thermal effect and focused on the pre-existing fractures. Wang et al. [19] constructed 3D THM model of fractured reservoir to simulate the hydro-shearing stimulation at the Utah FORGE site, but the borehole was also simplified and considered stimulation scenarios were limited. There are other works that included the real borehole to study the near-borehole fracture initiation and propagation, such as Zhang et al. [20], Xi et al. [21] and Wei et al. [22]. However, their models were limited to very small scales (cm). In brief, a model that can simultaneously consider coupled THM processes, fatigue damage, and the initiation and propagation of fractures on a realistic scale is rarely reported. The major challenges include modelling both conductive and convective heat transfer in the rock matrix and the growing fractures, which can cause numerical instability due to high Peclet number and introduce artificial compliance. In addition, the simulation of the fracture initiation and propagation under fully THM coupling can largely increase the computational burden. Therefore, a smart and flexible inclusion of the fracture growth is necessary.

This study aims to gain new insights into the mechanisms and effectiveness of various stimulation strategies (monotonic, stepwise, cyclic and stepwise combined with cyclic stimulation) in the presence of near-borehole clogging. In the following, the numerical method is briefed, followed by an introduction to the synthetic reservoir and the investigated scenarios. Results and discussions are then presented, followed by a conclusion.

2. Numerical method

2.1. Modelling approach

Modelling fracture behaviour in continuous porous media (e.g., rock) is a non-trivial task, as discontinuities break displacement compatibility of standard FEM formulations and pose strong singularities in the solutions. To mitigate these difficulties, zero-thickness interface elements, a conceptually simple technique, are used to represent the discontinuities in this work. Interface elements are inserted in between continuum elements to represent pre-existing or potential fractures, as shown in Fig. 2. A 2D modelling approach is used, with each interface element having in total 9 nodes, equally distributed on top, mid, and bottom planes (Fig. 2(b)). For an unloaded interface element, these three planes coincide in the same position.

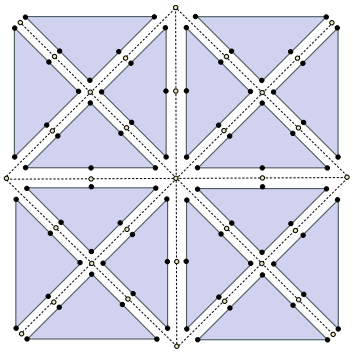

(a) Insertion of interface elements in between continuum elements (light blue).

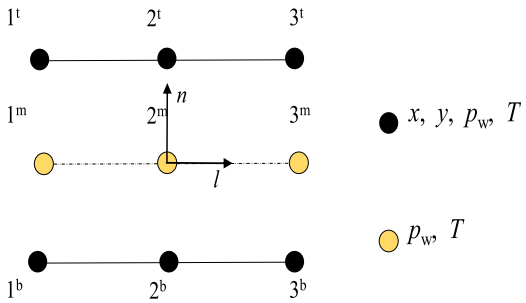

(b) Interface element

Fig. 2. Finite elements used. (a) Interface elements in between continuum elements to represent pre-existing or potential cracking paths, and (b) Element node numbering, nodal degrees of freedom and local basis.

The bottom and top faces of the interface element share nodes with the continuum element, with each shared node possessing four degrees of freedom, namely x and y coordinates, water pressure p_w, and temperature T. In contrast, the mid-plane nodes include only two degrees of freedom, namely the water pressure p_w and temperature T. In this way, different constitutive laws can be used for the continuum and the discontinuities, allowing for a more realistic representation of the heat and fluid fluxes along and across the fracture. The nodes of the bottom and top faces of the interface which are in contact with each other are pre-determined to both improve robustness and decrease computation. This, however, reduces the amount of shear displacement possible.

In this work, the thermal processes is included in the interface element, under the assumptions that the material is always water saturated (i.e., without considering a gas phase). Additionally, the water viscosity is dependent on temperature while water density is dependent on both water pressure and temperature. In the following section, the mathematical formulations for both the continuum and discontinuities are described. The formulations are implemented in the FEM code LAGAMINE [23], in which the formulation of continuum was implemented by Collin et al. [24] and the formulation of the interface element was implemented by Liaudat et al. [25] and Luo et al. [26]. The extensive verifications and validations of the proposed methods can be found in Luo et al. [26] and in Luo [27], and are not repeated here.

2.2. Governing equations for the continuum porous medium

The governing equations follow the formulation proposed by Collin et al. [24] Here the equations with corresponding constitutive laws are briefly introduced.

2.2.1. Hydraulic problem

The water mass balance equation without any internal source or sink reads:

$$\frac{\partial(\phi\rho_w)}{\partial t} + \nabla\cdot(\rho_w \mathbf{v}_w) = 0 \tag{1}$$

where ϕ is the porosity, ρ_w [kg/m^3] is the water density, and $\mathbf{v}_w$ [m/s] is the Darcy velocity vector. The latter is defined as:

$$\mathbf{v}_w = -\frac{\boldsymbol{K}}{\mu_w}\nabla p_w \tag{2}$$

where $\boldsymbol{K}$ [m^2] is the intrinsic permeability tensor and μ_w [Pa s] is the water dynamic viscosity.

Assuming isotropy, the intrinsic permeability tensor is defined as $\boldsymbol{K} = K\mathbf{I}$, where K is the scalar permeability and $\mathbf{I}$ is the identity tensor. Permeability is assumed to be a function of porosity according to:

$$K = K_0 \frac{(1-\phi_0)^m}{\phi_0^n}\frac{\phi^n}{(1-\phi)^m} \tag{3}$$

where K_0 [m^2] is the permeability for $\phi = \phi_0$. n is assumed to be 3 and m to be 2 [28].

In the above-mentioned equations, the properties of water are a function of temperature and water pressure. Accordingly, the water density and dynamic viscosity [29] are calculated as:

$$\rho_w = \rho_{w0}\left[1 + \frac{p_w - p_{w0}}{\kappa_w} - \beta_w\left(T - T_0\right)\right] \tag{4}$$

and

$$\mu_w = 0.6612(T-229)^{-1.562} \tag{5}$$

where ρ_{w0} [kg/m^3] is the water density defined at the reference pressure p_{w0} [Pa] and temperature T_0 [K], κ_w [1/Pa], the water compressibility, and β_w [1/K], the thermal expansion coefficient.

2.2.2. Mechanical problem

If equilibrium state is assumed and if gravity is neglected, the equation of momentum conservation reads:

$$\nabla\cdot\boldsymbol{\sigma} = \mathbf{0} \tag{6}$$

where $\boldsymbol{\sigma}$ [Pa] is Cauchy's total stress tensor.

The considered mechanical constitutive law for the bulk rock is the classical law [30]. If compressive stress and strain are defined as negative, the thermo-poro-elastic constitutive law reads:

$$\Delta\boldsymbol{\sigma} = \mathbb{C} : \Delta\boldsymbol{\epsilon} - \Delta p_w \mathbf{I} - \beta_b K_b \Delta T \mathbf{I} \tag{7}$$

where $\mathbb{C}$ is the 4th-order elastic stiffness tensor, $\boldsymbol{\epsilon}$ is the strain tensor, α is the Biot coefficient, $\mathbf{I}$ is the 2nd-order identity tensor, β_b [1/K] is the bulk volumetric thermal expansion coefficient, and K_b [Pa] is the drained bulk modulus.

2.2.3. Thermal problem

Under the assumption of local thermal equilibrium, with no internal source or sink, the equation of energy conservation reads:

$$\frac{\partial[(\rho c_p)_b T]}{\partial t} + \nabla\cdot\boldsymbol{q}_T = 0 \tag{8}$$

where $(\rho c_p)_b = (1-\phi)(\rho c_p)_s + \phi(\rho c_p)_w$ is the bulk volumetric heat capacity (with c_p [J/(kg K)] being the phase specific heat capacity, ρ the phase density, and the subscripts s and w referring to the solid and the water phases, respectively), and $\boldsymbol{q}_T$ [J/(m^2 s)] is the heat flux vector. The latter is given by:

$$\boldsymbol{q}_T = -\lambda_b\nabla T + \rho_w c_{pw}\mathbf{v}_w\left(T - T_0\right) \tag{9}$$

where the first term corresponds to Fourier's law with the bulk thermal conductivity given by λ_b [J/(m s K)] $= (1-\phi)\lambda_s + \phi\lambda_w$, and the second term corresponds to the heat advection due to water flow.

2.3. Governing equations for the discontinuities

The mechanical and hydraulic governing equations for the interface elements are inherited from Liaudat et al. [25] with the gas phase being neglected. Additionally, the governing equations for thermal processes are included here. Note that the following equations are tailored for 2D problems.

2.3.1. Hydraulic problem

The mass balance for water in a differential volume of discontinuity wdl reads:

$$\frac{\partial}{\partial t}(w\rho_{\mathrm{w}}) + \frac{\partial q_{\mathrm{w}}^{\mathrm{l}}}{\partial l} - q_{\mathrm{w}}^{\mathrm{b}} - q_{\mathrm{w}}^{\mathrm{t}} = 0 \tag{10}$$

where w [m] is the width of the discontinuity, $q_{\mathrm{w}}^{\mathrm{l}}$ [kg/(m s)] is the longitudinal water mass flow, and $q_{\mathrm{w}}^{\mathrm{b}}$ and $q_{\mathrm{w}}^{\mathrm{t}}$ [kg/(m^2 s)] are the transversal water mass fluxes incoming to the discontinuity from surrounding continuum medium [25].

The mass fluxes in Eq. (10) can be expanded as:

$$q_{\mathrm{w}}^{\mathrm{l}} = \rho_{\mathrm{w}} v_{\mathrm{w}}^{\mathrm{l}}; \quad q_{\mathrm{w}}^{\mathrm{b}} = \rho_{\mathrm{w}} v_{\mathrm{w}}^{\mathrm{b}}; \quad q_{\mathrm{w}}^{\mathrm{t}} = \rho_{\mathrm{w}} v_{\mathrm{w}}^{\mathrm{t}} \tag{11}$$

where $v_{\mathrm{w}}^{\mathrm{l}}$ [m^2/s], $v_{\mathrm{w}}^{\mathrm{b}}$ [m/s] and $v_{\mathrm{w}}^{\mathrm{t}}$ [m/s] are the longitudinal and transversal (top and bottom) volumetric fluxes. These fluxes obtained from the following generalised Darcy's law:

$$v_{\mathrm{w}}^{\mathrm{l}} = -\frac{t^{\mathrm{l}}}{\mu_{\mathrm{w}}}\frac{\partial p_{\mathrm{w}}^{\mathrm{m}}}{\partial l}; \quad v_{\mathrm{w}}^{\mathrm{b}} = -\frac{k^{\mathrm{b}}}{\mu_{\mathrm{w}}}\breve{p}_{\mathrm{w}}^{\mathrm{b}}; \quad v_{\mathrm{w}}^{\mathrm{t}} = -\frac{k^{\mathrm{t}}}{\mu_{\mathrm{w}}}\breve{p}_{\mathrm{w}}^{\mathrm{t}} \tag{12}$$

where t^{l} [m^3] is the longitudinal hydraulic coefficient, k^{b} [m^2] and k^{t} [m^2] are the transversal permeability of the interface, $p_{\mathrm{w}}^{\mathrm{m}}$ [Pa] is the water pressure at the middle plane, and $\breve{p}_{\mathrm{w}}^{\mathrm{b}}$ [Pa] and $\breve{p}_{\mathrm{w}}^{\mathrm{t}}$ [Pa] are the transversal pressure jumps between the bottom and top face and the mid-plane, respectively. The transversal pressure drops are defined as:

$$\breve{p}_{\mathrm{w}}^{\mathrm{b}} = (p_{\mathrm{w}}^{\mathrm{m}} - p_{\mathrm{w}}^{\mathrm{b}}); \quad \breve{p}_{\mathrm{w}}^{\mathrm{t}} = (p_{\mathrm{w}}^{\mathrm{m}} - p_{\mathrm{w}}^{\mathrm{t}}) \tag{13}$$

where $p_{\mathrm{w}}^{\mathrm{b}}$ and $p_{\mathrm{w}}^{\mathrm{t}}$ are the water pressures at the bottom and top sides of the discontinuity.

The longitudinal hydraulic coefficient t^{l} is estimated using the Reynolds lubrication equation, which describes the laminar flow of an incompressible and Newtonian fluid flowing between two parallel plates [31]. It reads:

$$t^{\mathrm{l}} = \frac{r_{\mathrm{n}}^3}{12} + t_0^{\mathrm{l}} \tag{14}$$

where r_{n} [m] is the normal separation of the interface, and t_0^{l} [m^3] is the initial longitudinal hydraulic coefficient, which makes it possible to assign an initial longitudinal transmissivity to the discontinuity even if it is closed from the mechanical point of view. The longitudinal hydraulic coefficient t^{l}, defined in Eq. (11), plays the same role in the hydraulic governing equations of the discontinuity as the intrinsic permeability $\boldsymbol{K}$ in the hydraulic governing equations of the continuum. Both parameters account only for the geometrical characteristics of the medium through which the liquid fluxes, i.e., they are independent of the fluid properties. The fluid properties (as well as the time dimension) are introduced via the water dynamic viscosity μ_w in Eqs. (2) and (9), for the continuum and discontinuities, respectively.

The width w will evolve with the normal separation of interface r_{n}:

$$w = r_{\mathrm{n}} + w_0 \tag{15}$$

where w_0 [m] can be set to be non-zero to assign an initial storage volume to the discontinuity even if it is mechanically closed [25].

2.3.2. Mechanical problem

The equation of momentum conservation for the interface element reads as follows:

$$\frac{\partial \boldsymbol{\sigma}_{\mathrm{c}}}{\partial l} = \mathbf{0} \tag{16}$$

where l is the longitudinal axis of the interface element, and $\boldsymbol{\sigma}_{\mathrm{c}} = [\sigma_{\mathrm{n}}, \sigma_{\mathrm{l}}]$ [Pa] is the total stress on the interface mid-plane, with σ_{n} and σ_{l} being the normal and shear stress components on that plane. In this paper, mode I fracturing is considered. The shear stress component is therefore not discussed here.

For the mechanical constitutive behaviour of the discontinuity, the bilinear traction–separation law schematically depicted in Fig. 3 is used [25,32]. More advanced constitutive laws can be incorporated easily into the code. This bilinear law can describe fracture behaviours characterised by six parameters: the maximum tension or shear strength σ_{n0} [Pa] or σ_{l0} [Pa], the normal or shear "cracking" separation r_{n0} [m] or r_{l0} [m], and the normal or shear debonding separation r_{nc} [m] or r_{lc}. Conventionally, the stress paths are represented by the black lines with the un-loading path represented by the black dashed lines in tensile and shear branches depicted respectively in Figs. 3(a) and 3(b). The tensile branch is modified to take into account the fatigue damage. After m cycles, the stress path is represented by the blue line in Fig. 3(a), showing that the tensile strength is reduced from σ_{n0} to σ_{nm}. When the cycle number reaches the fatigue life (the number of cycles a material can withstand before failure under a given loading amplitude) of the material, M_{f}, the tensile strength is further reduced to σ_{nMf}. Any loading below the threshold strength σ_{nMf} will not induce damages to the material no matter how many cycles are implemented.

In the loading condition, the normal and tangential (to the mid-plane of the interface element) stresses are given by the following expressions:

$$\sigma_{\mathrm{n}}' = \begin{cases} (1-D)K_{\mathrm{nm}} r_{\mathrm{n}} & \text{if } r_{\mathrm{n}} \geq 0 \\ K_{\mathrm{n0}} r_{\mathrm{n}} & \text{if } r_{\mathrm{n}} \leq 0 \end{cases} \tag{17}$$

$$\sigma_{\mathrm{l}} = (1-D)K_{\mathrm{l0}} r_{\mathrm{l}} \tag{18}$$

where σ_{n}' [Pa] represents Terzaghi's effective normal stress, defined as $\sigma_{\mathrm{n}}' = \sigma_{\mathrm{n}} + p_{\mathrm{w}}^{m}$, and $K_{\mathrm{n0}} = \sigma_{\mathrm{n0}}/r_{\mathrm{n0}}$ [Pa/m] is the initial normal slope. $K_{\mathrm{nm}} = \sigma_{\mathrm{nm}}/r_{\mathrm{n0}}$ is the normal stiffness after mth cycles and $\sigma_{\mathrm{nm}} = (1-D_{\mathrm{f}})\sigma_{\mathrm{n0}}$. D_{f} is the fatigue damage variable and will be defined later. σ_{l} and r_{l} are the tangential stress and separation respectively, and $K_{\mathrm{l0}} = \sigma_{\mathrm{l0}}/r_{\mathrm{l0}}$ is the tangential slope. When an interface element is used to represent natural fractures, the normal slope can have a physical meaning, interpreted as fracture stiffness, for instance, as a result of interpenetration of fracture surfaces due to presence of asperities [33,34]. In the context of this paper, K_{n0} is interpreted as penalty coefficients, thus allowing negligible interpenetration of fracture surfaces regardless of their roughness [33]. To enforce the contact constraints, the slope should be set high enough to reduce artificial compliance [25]. However, the choice of their values is a trade-off between having artificial compliance and having numerical convergence problems. Additionally, D is the damage variable ranging from 0 (intact rock) to 1 (fully separated fracture). This damage variable evolves as follows:

$$D = \min\left(\frac{\bar{\omega}}{1+\bar{\omega}}\frac{1}{\eta}, 1\right) \tag{19}$$

$$\bar{\omega} = \max(\omega) \tag{20}$$

$$\omega = \left\langle \left(\frac{\langle r_{\mathrm{n}} \rangle}{r_{\mathrm{n0}}}\right)^{\beta} + \left(\frac{|r_{\mathrm{l}}|}{r_{\mathrm{l0}}}\right)^{1/\beta} - 1 \right\rangle \tag{21}$$

$$\eta = 1 - \frac{r_{\mathrm{n0}}}{r_{\mathrm{nc}}} = 1 - \frac{r_{\mathrm{l0}}}{r_{\mathrm{lc}}} \tag{22}$$

where ω is a positive scalar that defines the mechanical degradation of the interface element for a given normal separations, $\bar{\omega}$ is a history variable that stores the maximum value reached by ω during the

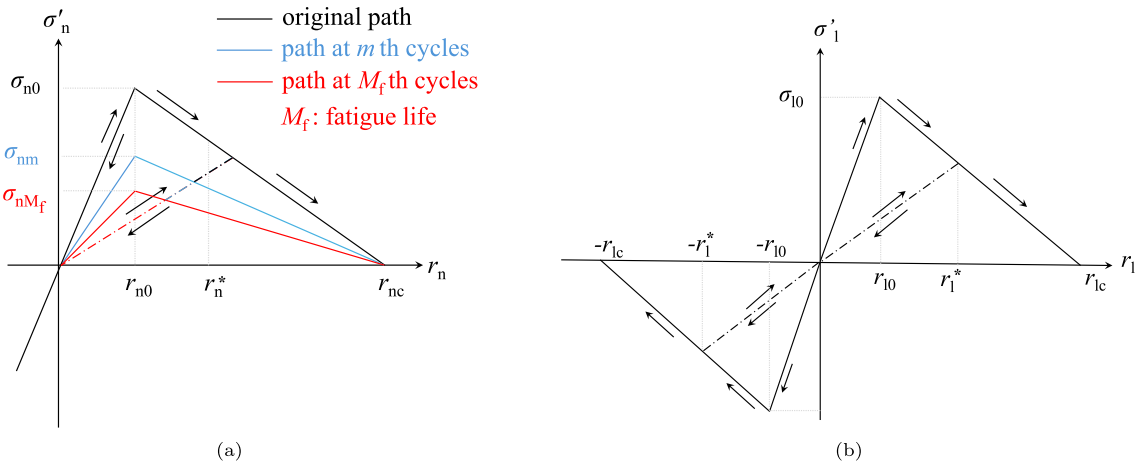

Fig. 3. The elasto-damage law. (a) Tensile branch incorporating the fatigue damage; (b) Shear branch.

loading history, and $\langle\cdot\rangle = (\cdot + |\cdot|)/2$ is the Macaulay bracket. β is a material parameter that characterise the mixed mode damage and is assumed to be 1 in this work [25]. The above equations state that if the separation r_n is less than the normal crack separation r_{n0}, the damage variable D is then zero. If $r_{n0} < r_n < r_{nc}$, D is between 0 and 1, determined by the ratio of $(r_n - r_{n0})/(r_{nc} - r_{n0})$. Otherwise if r_n is beyond the debonding separation r_{nc}, D is forced to be 1, indicating a completely separation of the interface element.

To determine the fatigue damage variable, a linear strength degradation is assumed [21,35]. Thus, when subjected to constant-amplitude cyclic loading (Fig. 4(a)), it is defined as:

$$D_f = \left(1 - \frac{\sigma'_A}{\sigma_{n0}}\right)\frac{m}{M_f} \tag{23}$$

where σ'_A [Pa] is the amplitude of the cyclic loading (effective stress). M_f is the fatigue life (maximum number of cycles until failure) under a specific constant-amplitude cyclic loading.

When subjected to varying-amplitude cyclic loading shown in (Fig. 4(b)), Eq. (23) can be further developed based on the Palmgren-Miner's rule, which reads:

$$D_f = \sum_i \left(1 - \frac{\sigma'_{Ai}}{\sigma_{n0}}\right)\frac{1}{M_{fi}} \tag{24}$$

where i indicates the ith cyclic loading that has a maximum amplitude of σ'_{Ai}, as shown in Fig. 4(b). M_{fi} is the fatigue life corresponding to the applied loading level σ'_{Ai}.

An empirical S-N relationship is used as a criterion to determine the fatigue life M_{fi}, which relates the maximum value of the cyclic loading (σ'_{Ai}) to the fatigue life M_{fi} of the rock. This relationship has been widely used in metals, concrete, and rocks [21,35–37]. It reads [21,37]:

$$\frac{\sigma'_{Ai}}{\sigma_{n0}} = a\log_{10} M_{fi} + b \tag{25}$$

where a and b are model parameters that can be determined from experimental data.

Moreover, mechanical viscosity is added to the contact stress to resolve the solution jump that can result in numerical divergence [25,38]:

$$\sigma'_n = \sigma_n + p_w^m + \sigma_v \qquad \text{with} \quad \sigma_v = \zeta\frac{\partial r_n}{\partial t} \tag{26}$$

where ζ [Pa s/m] is the viscosity added to resolve large fast changes in the solution, which occur faster than the time discretisation, and can cause numerical divergence. The added viscosity ζ slows down the strain rate and thus stabilised the solution. Detailed discussion on the solution jumps and how the added viscosity helps mitigate this issue can be found in other works [25,38].

2.3.3. Thermal problem

The conservation of energy, in terms of temperature, applied to a differential volume of discontinuity wdl reads:

$$\frac{\partial}{\partial t}\left(w\rho_w c_{pw} T^m\right) + \frac{\partial q_T^l}{\partial l} - q_T^b - q_T^t = 0 \tag{27}$$

where q_T^s [J/(m^2 s)] is the rate of change of the heat stored in the discontinuity, q_T^l [J/(m s)] is the longitudinal heat flux, q_T^b [J/(m^2 s)] and q_T^t [J/(m^2 s)] are the normal heat fluxes incoming from the surrounding continuum medium via bottom and top faces to the discontinuity, respectively.

The terms in Eq. (27) can be expanded as:

$$q_T^l = -w\lambda_w\frac{\partial T^m}{\partial l} + c_{pw}q_w^l T^m \tag{28}$$

$$q_T^b = -\lambda_w\frac{2\check{T}^b}{\max(w,\bar{w})} + c_{pw}q_w^b\check{T}^b \tag{29}$$

$$q_T^t = -\lambda_w\frac{2\check{T}^t}{\max(w,\bar{w})} + c_{pw}q_w^t\check{T}^t \tag{30}$$

where $\check{T}^b = T^m - T^b$ and $\check{T}^t = T^m - T^t$ are the temperature jumps between the bottom or top face and the mid-plane, with T^m, T^b and T^t being the temperatures at the mid-plane, bottom and top face of interface element, respectively, and λ_w is the thermal conductivity of the water. $\bar{w}$ is a penalty coefficient to avoid singularity when interface elements are used to provide potential cracking paths in intact rock. The penalty coefficient should be as small as possible to reduce the artificial compliance.

3. Synthetic reservoir with clogged near-borehole area

The potential of stimulation is analysed on a synthetic case of a sandstone reservoir with clogged near-borehole zone. The synthetic reservoir is assumed to be a non-fractured sandstone reservoir, inspired by the Delft Sandstone Formation. A borehole with a radius of 0.2 m is located at the centre of a circular domain with a radius of 500 m (to ensure no boundary effects) and a thickness of 100 m. A near-borehole zone with a radius of 5 m is assumed to be clogged, with impaired permeability decreasing to 1% of the initial reservoir permeability K_0. Clogging with a (much) smaller distance from the borehole wall could exist, but in this case, either chemical or mechanical means could probably be used to rehabilitate the well. Therefore, a reasonably extreme case has been selected. Anisotropic clogging pattern is likely existing due to actual drilling intrusion and mineral dissolution/precipitation. Yet isotropic clogging is assumed in this work for simplicity.

Representative reservoir data is collected from the TU Delft campus geothermal project. Comprehensive data has been collected during the

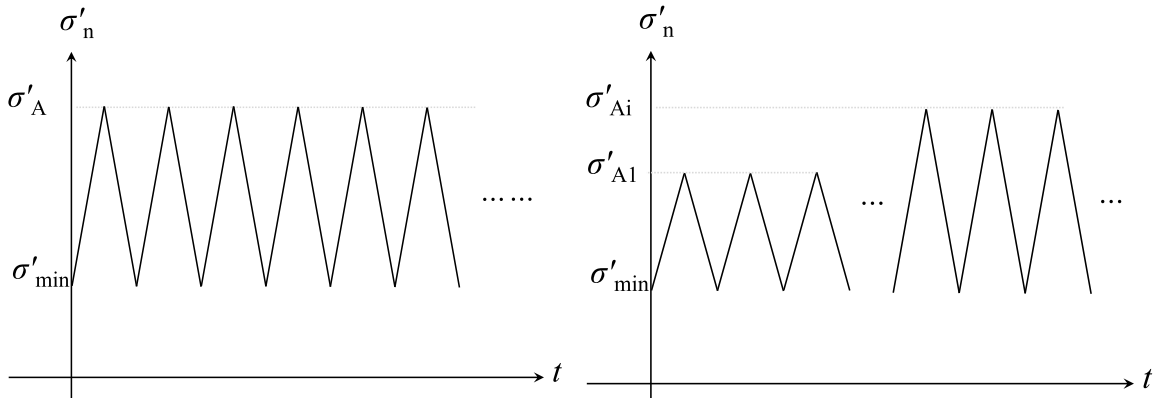

(a) Cyclic loading with constant amplitude. (b) Cyclic loading with varying amplitude.

Fig. 4. Different loading scenarios.

Table 1
Reservoir data for the exploratory analyses, based on the Delft Sandstone Formation [39,41–43].

Parameter	Symbol	Value	Unit
Reservoir thickness	H_r	100	m
Total vertical stress	σ_v	48	MPa
Total maximum horizontal stress	σ_H	42	MPa
Total minimum horizontal stress	σ_h	38	MPa
Initial reservoir pressure	p_{wi}	21	MPa
Initial reservoir temperature	T_i	353	K
Reservoir porosity	ϕ	0.17	–
Solid density	ρ_s	2650	kg/m^3
Reservoir permeability	K	1.6×10^{-12}	m^2
Impaired permeability	K'	1.6×10^{-14}	m^2
Young's modulus	E	11.5	GPa
Poisson's ratio	ν	0.15	–
Unconfined compressive strength	σ_c	48	MPa
Tensile strength[a]	σ_t	4.8	MPa
Internal friction coefficient	μ	0.75	–
Volumetric thermal expansion coefficient	β	6.5×10^5	1/K
Thermal conductivity	λ	3	W/(m K)
Specific heat capacity	c_{ps}	924.5	J/(kg K)

[a] σ_t is assumed to be 1/10 of σ_c, which is derived from logging data.

drilling of the doublet [39,40], including from cores and a large suite of open-hole well logs in the reservoir section of both wells. With regional knowledge, the data from the doublet and surrounding wells, a normal faulting regime can be assumed. Logging data and regional knowledge allows an estimation of the pore pressure to be around 21 MPa and in-situ stresses to be σ_v = 48 MPa, σ_H = 42 MPa and σ_h = 38 MPa, at depth of 2000 m. According to regional studies, the azimuth of the σ_H is between N130°E and N150°E. After drilling, the well DEL-GT-01 has been tested by means of a gas-lift, providing valuable information of the reservoir quality, such as permeability and temperature. In addition, previous oil and gas explorations and other nearby geothermal projects provide a large dataset including hydraulic, thermal and mechanical properties [41,42]. The properties used in exploratory analysis are summarised in Table 1.

4. Numerical model

4.1. Geometry and mesh

To simulate the near-borehole coupled processes under thermo-hydraulic stimulation in the synthetic reservoir, a symmetric plane strain 2D horizontal model with a domain radius of 500 m is constructed, shown in Fig. 5(a). The domain is composed of 3 material groups with radius from (0.2 m–5 m), (5 m–10 m) and (10 m–500 m) respectively, in order to assign different properties to the clogged zone (0.2 m–5 m) and unclogged zone (5 m–500 m), and to insert interface elements only in the near-borehole domain (0.2 m–10 m). A borehole with radius of 0.2 m is placed at the centre.

The model is meshed with 2nd-order triangular continuum elements, with interface elements inserted in between all the continuum elements within the inner region from 0.2 m–10 m radius to enable arbitrary fracture initiation and propagation near the borehole (see Fig. 5(b)). This approach ensures reasonable reservoir performance taking into account the far-field behaviour while minimising computational and memory demands by avoiding interface elements throughout the entire domain. As shown in [26], insertion of interface elements in between continuum elements to provide potential cracking paths in intact rock will introduce artificial compliance that have an impact on thermo-hydro-mechanical response. To reduce the mechanical artificial compliance, the stiffness of the interface elements is set as high as possible without causing numerical difficulties, i.e. a lack of convergence, as discussed in [26]. The hydraulic and thermal artificial compliances can be reduced in a similar way, by assigning a high transversal transmissivity of the interface element to reduce the flow resistance. The detail of reducing the hydraulic and thermal artificial compliances is presented in the Appendix.

4.2. Initial and boundary conditions

The initial stresses are σ_h = 38 MPa in x direction and σ_H = 42 MPa in y direction. The displacements normal to the symmetry axis (bottom as shown in Fig. 5(a)) are fixed in the y direction, while the displacement is fixed in both x and y directions along the far-field boundary. A uniform normal load, which is equal to the steady-state injection pressure, is distributed around the borehole throughout the simulation time, leading to a zero effective stress around the borehole. In addition to the mechanical boundary conditions, temperature and fluid pressure are fixed to their initial values at the far-field boundary. A monotonic q_{2D} (kg/(m s)), leading to a total injection rate Q_{inj} (m^3/h, = $2 \times 3600 \times H_r \times \rho_w \times q_{2D}$) for the open-hole section with thickness of H, is applied on an environment node, which is connected to the borehole nodes without resistance to mimic the well-bore. The temperature at the borehole wall is fixed at the injection temperature T_{inj}. Note that the heat exchange between the wellbore fluid, casing and the formation is not included in this model, and could overestimate the thermally-induced stresses.

4.3. Input parameters

A linear elastic model is used for the continuum elements, while the previously developed elasto-damage law that incorporates the fatigue

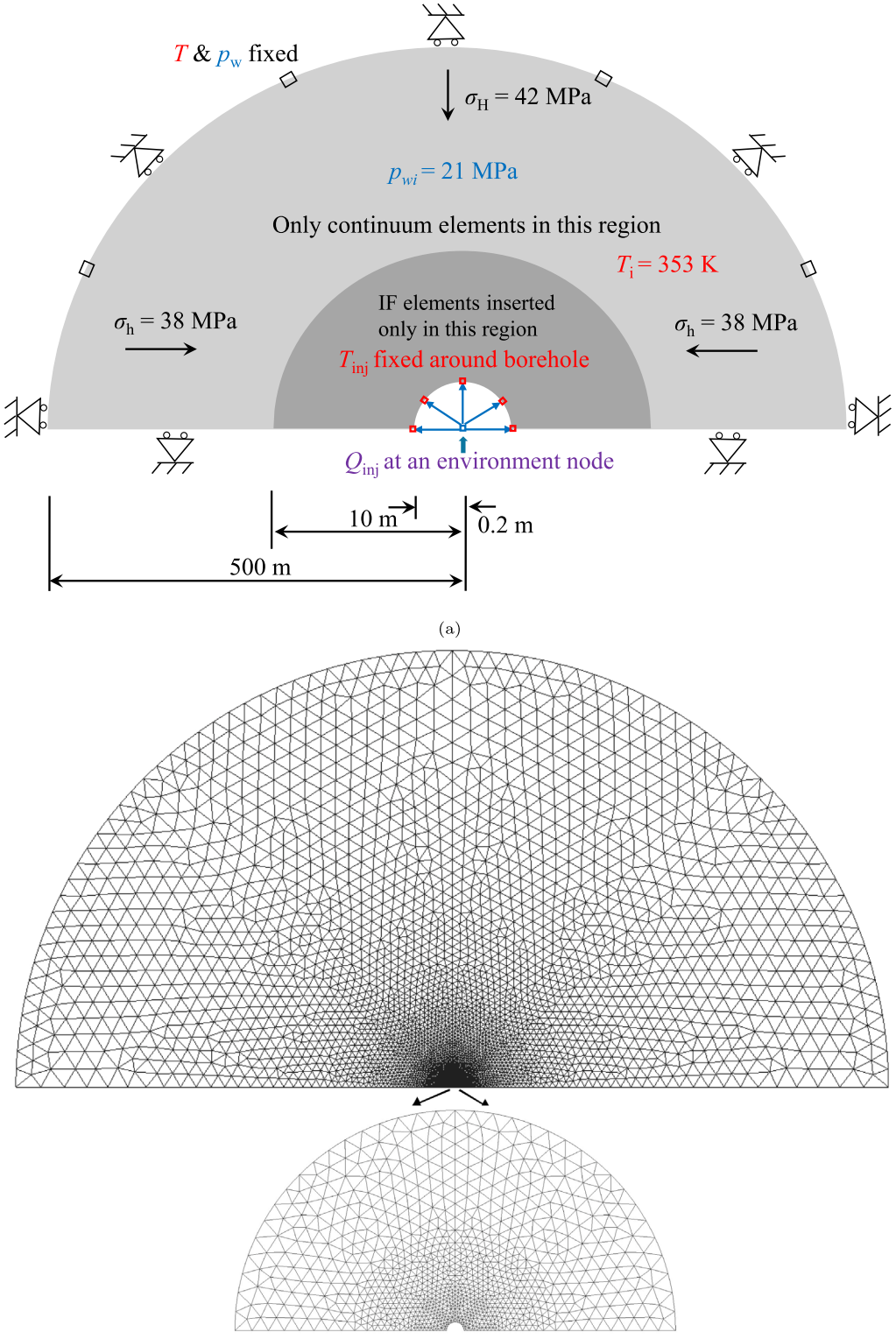

Fig. 5. Schematic of the (a) Numerical model domain with boundary conditions. Not to scale. An environment node is used to mimic the wellbore, on which the injection rate is applied. The environment node is connected with the borehole nodes without flow resistance. Interface (IF) elements are inserted in bewteen all the continuum elements within the inner region from 0.2 m–10 m radius (the dark grey region). Outside this region, only continuum elements are used; and (b) meshing of the domain.

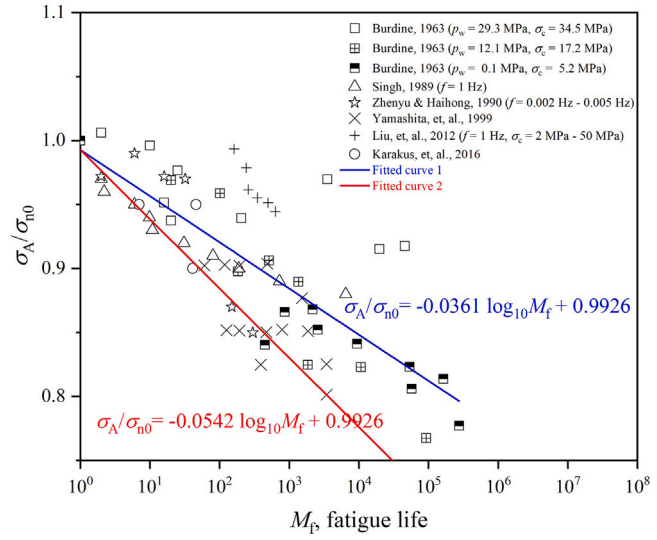

Fig. 6. S-N relationship determined by fitting the experimental data collected from the literature.

Table 2
Input parameters for the interface elements used in the model.

Parameter	Symbol	Value	Unit
Tensile strength	σ_{n0}	4.8	MPa
Tensile cracking separation	r_{n0}	10^{-7}	m
Tensile debonding separation	r_{nc}	10^{-6}	m
Shear strength	σ_{l0}	32	MPa
Shear cracking separation	r_{l0}	10^{-7}	m
Shear debonding separation	r_{lc}	10^{-6}	m
Mechanical viscosity	ζ	10^{14}	Pa s/m
Parameter a	a	−0.0361	–
Parameter b	b	0.9926	–
Initial aperture	w_0	10^{-5}	m
Initial longitudinal transmissivity (non-clogged)	t_0^l	1.6×10^{-17}	m^3
Initial longitudinal transmissivity (clogged)	t_0^l	1.6×10^{-19}	m^3
Initial transversal transmissivity (in both cases)	$t_0^{b/t}$	10^{-10}	m^3
Stabilisation coefficient	$\delta \cdot h$	10	m

δ is the tuning parameter and h is the element length.
They are used in both longitudinal and transversal heat transfer in the interface elements to stabilise the numerical solution.

damage into the tensile branch is used for the interface elements. The parameters assigned to the continuum elements are presented in Table 1, while the parameters for the interface elements are summarised below in Table 2. Note that the initial longitudinal transmissivity of the interface element is determined as equivalence to the impaired permeability of the continuum element [26], while the transversal transmissivity is set high to reduce the artificial compliance.

The parameters a and b that describe the S-N relationship are determined by fitting the experimental data collected from literature. All the strength used was measured using sandstone rock samples. The fitting curve is shown in Fig. 6.

5. Investigated scenarios

The model including interface elements (with stabilisation and interface element parameters selected for accuracy) will be used to study various synthetic stimulation scenarios with fully coupled THM processes and fatigue damage considered, allowing fracture initiation and propagation. Different stimulations, including monotonic, stepwise injection rate, cyclic injection rate or temperature stimulation and stepwise combined with cyclic rate stimulation scenarios will be simulated based on the reservoir with clogged near-borehole zone (assuming a clogged radius of 5 m where the permeability is reduced to 0.01 K_0) to evaluate the stimulation performance of different stimulation strategies. Considering the large computational burden and the soft stimulation practice performed in Pohang geothermal field [4], the total operation period is restricted in 5 days. Table 3 summarises the investigated scenarios, which are further detailed below.

The simulation of different stimulation scenarios for a synthetic reservoir with clogged near-borehole zone are then carried out. First, monotonic injection of cold water with different injection rates, labelled as $M1$ (Q_{inj} = 360 m^3/h), $M2$ (Q_{inj} = 288 m^3/h), $M3$ (Q_{inj} = 216 m^3/h) and $M4$ (Q_{inj} = 54 m^3/h), are first simulated. Based on scenario $M1$, the simulations of coupled hydro-mechanical (H-M), thermo-hydraulic (T-H) and fully coupled THM processes are compared to highlight the influence of the temperature and the initiation and propagation of fractures. In addition, the effects of different injection temperatures (ΔT = 35 K, 40 K, 45 K) are further discussed, with simulations based on $M2$.

Secondly, two stepwise stimulations, as is shown in Fig. 7(a) (labelled as $S1$) and Fig. 7(b) (labelled as $S2$), are investigated with ΔT fixed at 40 K.

Thirdly, different cyclic stimulations, as is shown in Fig. 7(c) (labelled as $C1$) and Fig. 7(d) (labelled as $C2$ or $C3$), are investigated. Scenario $C1$ represents the injection temperature is cycled with fixed injection rate, while scenarios $C2$ and $C3$ represent the injection rate is cycled with fixed injection temperature. For scenario $C1$, the ΔT is cycled between 0 K and 40 K, with injection rate fixed at 216 m^3/h. In one complete cycle, the ΔT is first kept at 40 K for a period of Δt, which can be 5 h or 10 h, and then changed to 0 K for $0.9\Delta t$, which is chosen to avoid numerical divergence (happens if keeping ΔT = 0 K for Δt) while keeping enough time for the reservoir to warm up. In contrast, for scenarios $C2$ and $C3$, the maximum injection rate is either 54 m^3/h or 216 m^3/h respectively, while the minimum injection rate is $Q_{inj}^{max}/10$ instead of shut in (for numerical convergence and practical reasons, e.g. to avoid the largest seismic events which have been observed during shut-in [4,44,45]), with the ΔT fixed at 40 K. In one complete cycle, the injection rate is first kept at its maximum Q_{inj}^{max} (= 216 m^3/h or 54 m^3/h) for a period of $\Delta t'$, which can be 6 min or 12 min, and then the injection rate decreases to Q_{inj}^{min} (= $Q_{inj}^{max}/10$), which is kept for $\Delta t'/2$. Note that the Δt is much larger than $\Delta t'$ since the heat transfer is much slower than hydraulic process.

Fourthly, a combination of cyclic and stepwise stimulation strategy is investigated, as is shown in Fig. 7(e) (labelled as $CS1$) and Fig. 7(f) (labelled as $CS2$). Scenario $CS1$ is a combination of cyclic injection rate and the stepwise scenario $S1$, while scenarios $CS2$ is a combination of cyclic injection rate and the stepwise scenario $S2$. The injection temperature is fixed in both scenarios.

6. Results and discussion

6.1. Reservoir with near-borehole clogging: monotonic stimulation ($M1$–$M3$)

This section considers the response of the reservoir with near-borehole clogging to constant injection with different rates and temperatures. To compare results, an average damage variable ($\bar{D}$) is defined as the average value of damage variables over the interface elements along a line through the 5 m radius clogged zone in the direction of the maximum initial stress σ_H, i.e. the location where the main fracture is expected to be induced and propagate. $\bar{D}$ can be used to indicate the length of the main fracture and therefore indicate if the main fracture breaks through the clogged zone. An average damage variable ($\bar{D}$) of 1 along this line indicates the main fracture breaks through the 5 m clogged area, thus connecting the wellbore and the un-clogged zone.

Fig. 8 compares the pressure response under fixed Q_{inj} = 360 m^3/h with consideration of coupled THM (with ΔT = 40 K), T-H (with ΔT = 40 K) and H-M (with ΔT = 0 K) processes in the simulations. Results

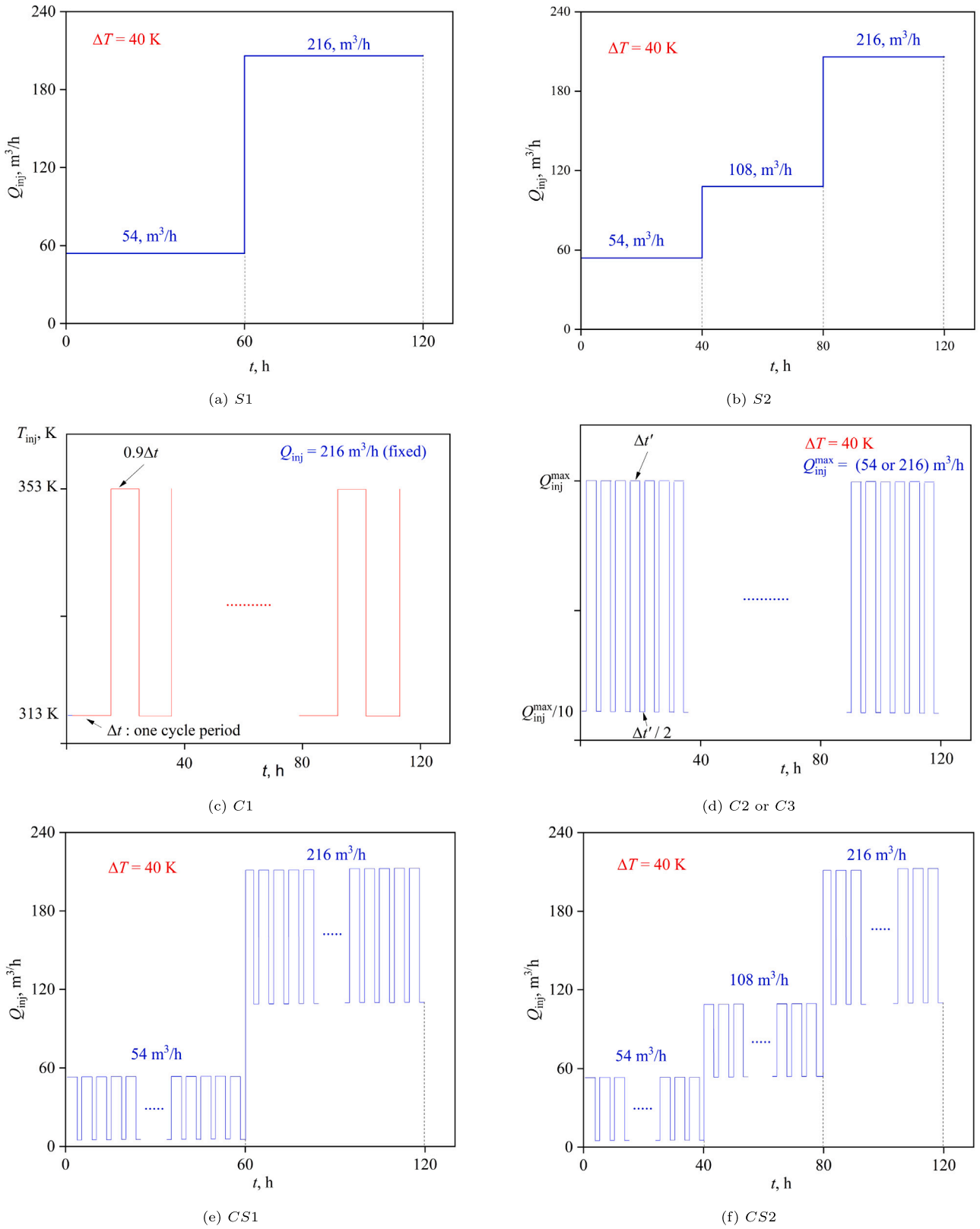

Fig. 7. Visualisation of the investigated scenarios. (a)–(b): Stepwise stimulation scenarios. Injection temperature is fixed at 313 K. (c): The cyclic injection temperature scenario $C1$, where Δt is the cycle period, which is either 5 h or 10 h. (d): The cyclic injection rate scenario $C2$ or $C3$, where $\Delta t'$ is the cycle period, which is 6 min or 12 min. Maximum injection rate is 54 m^3/h or 216 m^3/h, while the minimum injection rate is $Q_{inj}^{max}/10$, with injection temperature fixed at 313 K. (e)–(f): Combined cyclic and stepwise stimulation scenarios $CS1$ and $CS2$.

Table 3
Synthetic injection scenarios. The total injection time is 120 h. In each cycle of the scenario $C1$, the ΔT is kept at 40 K for Δt, which can be 5 h or 10 h, and then kept at 0 K for another 0.9 Δt. In each cycle of scenario $C2$ and $C3$, the Q_{inj} is kept at Q_{inj}^{max} for $\Delta t'$, which can be 3 min, 6 min or 12 min, and then kept at Q_{inj}^{min} for another 0.5$\Delta t'$.

Inj. scheme	Label	Inj. rate, Q_{inj} (m^3/h)	$\Delta T(K) = T_{inj} - T_i$
Monotonic	$M1$	360	0/40
	$M2$	288	35/40/ 45
	$M3$	216	40
	$M4$	54	40
Stepwise	$S1$	216 → 216 (each 60 h)	40
	$S2$	108 → 216 → 216 (each 40 h)	40
Cyclic T_{inj}	$C1$	216	40 (Δt) ↔ 0 (0.9Δt)
Cyclic Q_{inj}	$C2$	5.4 (0.5$\Delta t'$) ↔ 54 ($\Delta t'$)	40
	$C3$	28.8 (0.5$\Delta t'$) ↔ 216 ($\Delta t'$)	40
Cyclic + stepwise	$CS1$	(5.4 ↔ 54) → (54 ↔ 216)	40
	$CS2$	(5.4 ↔ 54) → (54 ↔ 108) → (108 ↔ 216)	40

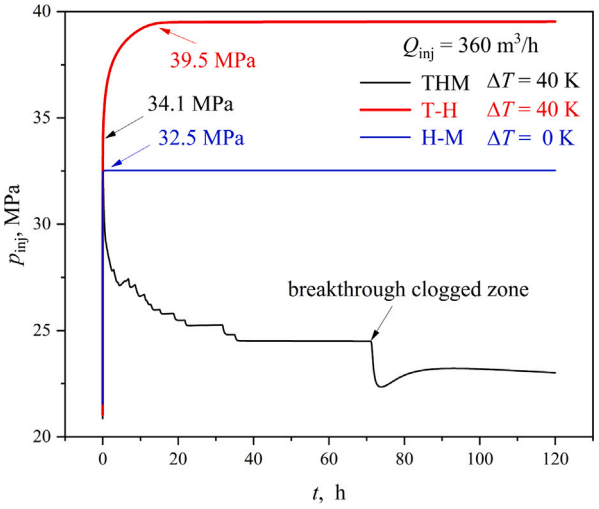

Fig. 8. Comparison of injection response under coupled THM, T-H, H-M simulations with Q_{inj} fixed at 360 m^3/h ($M1$ scenario).

show that the injection pressure reaches a constant value at 32.5 MPa quickly for the case of H-M simulation, indicating that steady state is reached quickly due to the fast pressure diffusion. In contrast, for the case of T-H simulation, the injection pressure keeps increasing to 39.5 MPa, at which the pressure remains approximately constant, as a result of the propagation of the cooling front, which increases the viscosity therefore flow resistance. If the fully coupled THM processes are considered, the injection pressure increases to 34.1 MPa, and then sharply and continuously decreases as a result of the initiation and propagation of near-borehole fractures. At approximately t = 65 h, there is a sudden and significant drop in the pressure, indicating that fracture(s) breaks through the clogged zone, and connects the wellbore and the un-clogged zone. The comparison highlights the importance of the consideration of the fully coupled THM processes and the initiation and propagation of fractures.

As shown in Fig. 9, in the $M1$ scenario (the fully coupled THM case), there is a main fracture propagating in the direction of the major principal stress and two symmetric fracture branches induced which are oriented around 45° and −45° (0° is defined to be in the North). To explain this phenomenon, Fig. 9 presents the fractures evolution with the distribution of the major principal stress σ_1 in the near-borehole zone, taking the case of Q_{inj} = 360 m^3/h and ΔT = 40 K as an example. In the first few hours, as is shown in Figs. 9(a)–9(c), small fractures are induced around the borehole due to the thermally-induced stress and hydraulic pressure. Although pore pressure and temperature changes act as isotropic scalar loads, the initial stresses and applied stresses lead to the strongest tensile stress to be in the direction of σ_H (i.e. y direction). Therefore, the main fracture opens first, pushing the side fractures to close. On the other hand, the stress concentration at the borehole wall due to both cold fluid injection causes further tensile stresses which remain lowest in the direction of σ_h and highest at the tip of the already opened fracture. In addition, the mesh also plays a role. The edges of the elements are radially intersecting the borehole in the direction of 45°, 90° and 135°, as shown in Fig. 5(b), in which the mesh is presented. In contrast, in other directions, the edges of the elements intersect with the borehole with an angle deviated from the radial direction. Therefore, the normal stress applied on these interface elements (edges) is lower than the major principal stress, and are unable to open the interface elements. Consequently, fracture branches find its easiest way to propagate in the direction of 45° and 135°, while fracture branches in other directions are closed. In comparison, Fig. 10 demonstrates the major principal stress distribution at different time steps under only H-M coupled. It shows that the stress is not changing, since hydraulic processes reach steady state in a short time. In addition, the major principal stress remains in compression without contribution from thermally-induced stress, and therefore no fracture happens. This highlights the importance of taking into account the thermal processes in geothermal reservoirs.

Fig. 11(a) compares the injection pressure and evolution of the averaged damage variable $\bar{D}$ for scenarios $M1$ to $M4$ with fully coupled THM processes under different injection rate Q_{inj} at fixed ΔT = 40 K. As is shown in Fig. 11(a), all simulations show substantial damage, with $\bar{D}$ reaching values well above 0.8 when the injection rate is 216 m^3/h, 288 m^3/h, and 360 m^3/h. The sudden drop in injection pressure at approximately t = 118 h and t = 70 h is observed for the cases of Q_{inj} is 288 m^3/h and 360 m^3/h respectively, with the corresponding $\bar{D}$ at 1, indicates a fracture fully penetrating the clogged area. If the injection rate is largely reduced to 54 m^3/h, the length of the fracture(s) is limited (as is shown in Fig. 12(a)), although damage is seen to continuously occur.

In addition, the pressure around the tip of the main fracture is built up when the Q_{inj} = 216 m^3/h (Fig. 12(b)) but relaxed in the clogged area when Q_{inj} = 288 m^3/h as a result of breaking through the damage area, as is shown in Fig. 12(c), while for the case of Q_{inj} = 360 m^3/h, the injection pressure is recovering (Fig. 12(d)) as the cold front moves further, though the main fracture breakthroughs the clogged area. For the other two cases (Q = 54 m^3/h and 216 m^3/h), no pressure relaxation happens since fracture is shorter and does not breakthrough the clogged area. A high peak of injection pressure at 28.9 MPa–34.1 MPa is observed when Q_{inj} is equal to or higher than 216 m^3/h, which is significantly higher than the injection pressure (21.5 MPa) for the unclogged reservoir, and could potentially increase the risk of seismicity as a result of the transient pressure pulse and equipment failure.

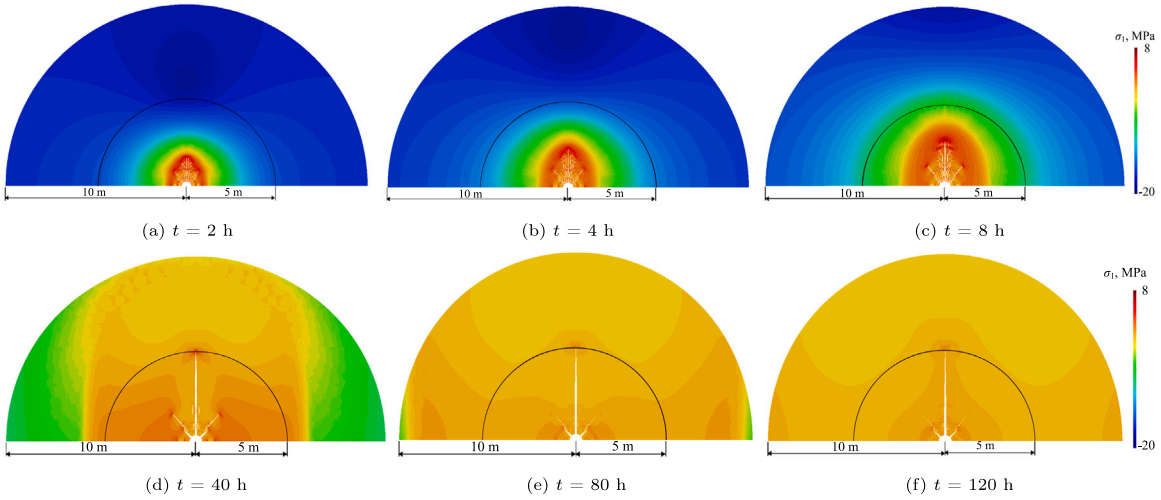

Fig. 9. Distribution of the major principal stress σ_1 at different time steps with deformed mesh under Q_{inj} = 360 m^3/h and ΔT = 40 K ($M1$ scenario). The legend range is −20 MPa (compressive) to 8 MPa (tensile). The deformation is 50 times enlarged, and only the domain within a radius of 10 m is shown.

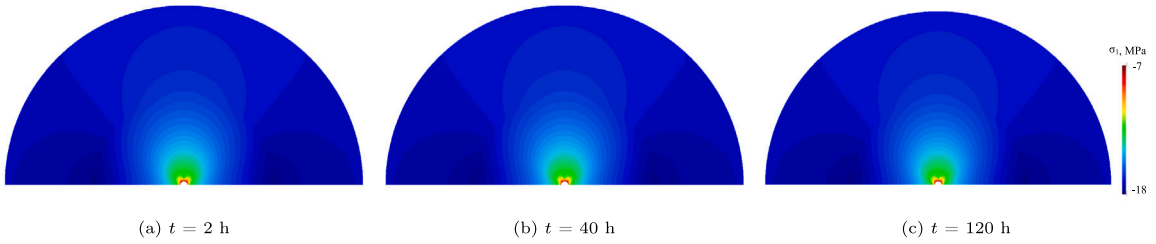

Fig. 10. Distribution of the major principal stress σ_1 at different time steps with deformed mesh under Q_{inj} = 360 m^3/h and ΔT = 40 K but with only hydro-mechanical (H-M) coupling. The legend range is −18 MPa (compressive) to −7 MPa (compressive). The deformation is 50 times enlarged, and only the domain within a radius of 10 m is shown.

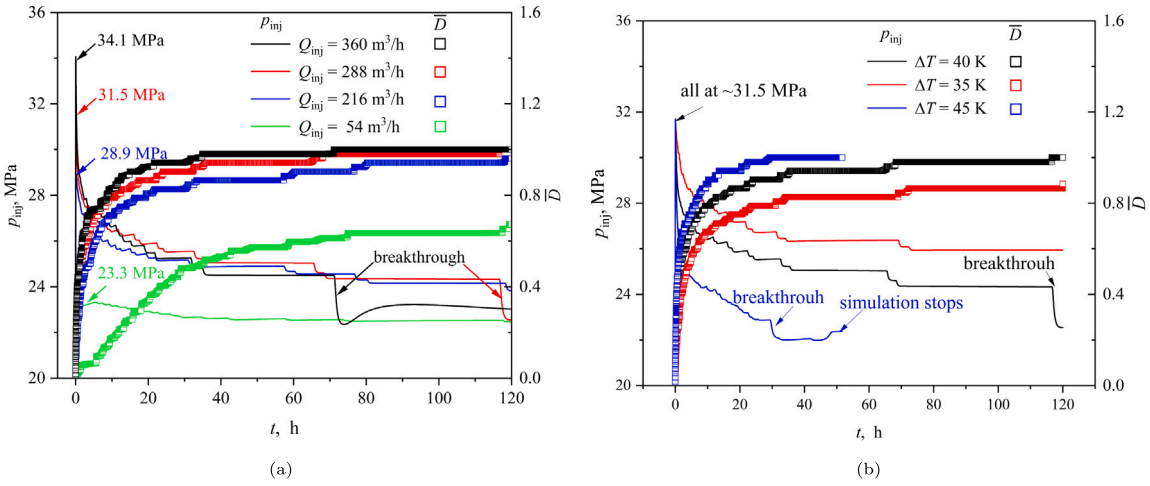

Fig. 11. Injection pressure and averaged damage variable evolution under (a) $M1$ to $M4$ scenarios, different injection rate with fixed ΔT = 40 K; and (b) $M2$ scenario different ΔT with fixed Q_{inj} = 288 m^3/h. The damage variable is averaged over the interface elements along a line through the 5 m clogged area from the borehole to the outer radius in the direction of the maximum initial stress σ_H.

Fig. 11(b) compares stimulation performance with different injection temperatures with the same injection rate ($M2$ scenario). The results show no significant difference in peak pressure, all at around 31.5 MPa, while a larger temperature difference of ΔT = 45 K and 40 K can result in earlier breakthrough of the clogged zone and lower injection pressure after reaching the peak pressure. This is because, as shown in Fig. 13(c), the large thermally-induced stress leads to a more damage around the borehole, even complete separation of some

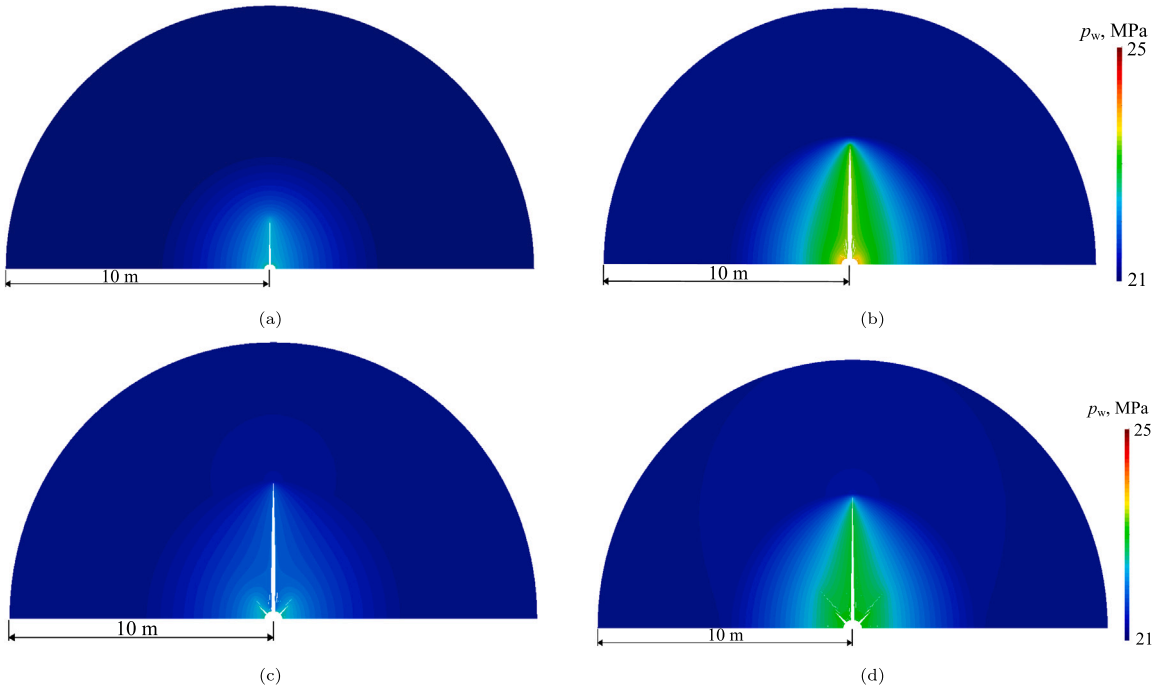

Fig. 12. Pressure distribution at t = 120 h with deformed mesh under different injection rate (ΔT is fixed at 40 K) - $M1$ to $M4$ scenarios. (a) Q_{inj} = 54 m^3/h; (b) Q_{inj} = 216 m^3/h; (c) Q_{inj} = 288 m^3/h; (d) Q_{inj} = 360 m^3/h. The deformation is 50 times enlarged, and only the domain within a radius of 10 m is shown.

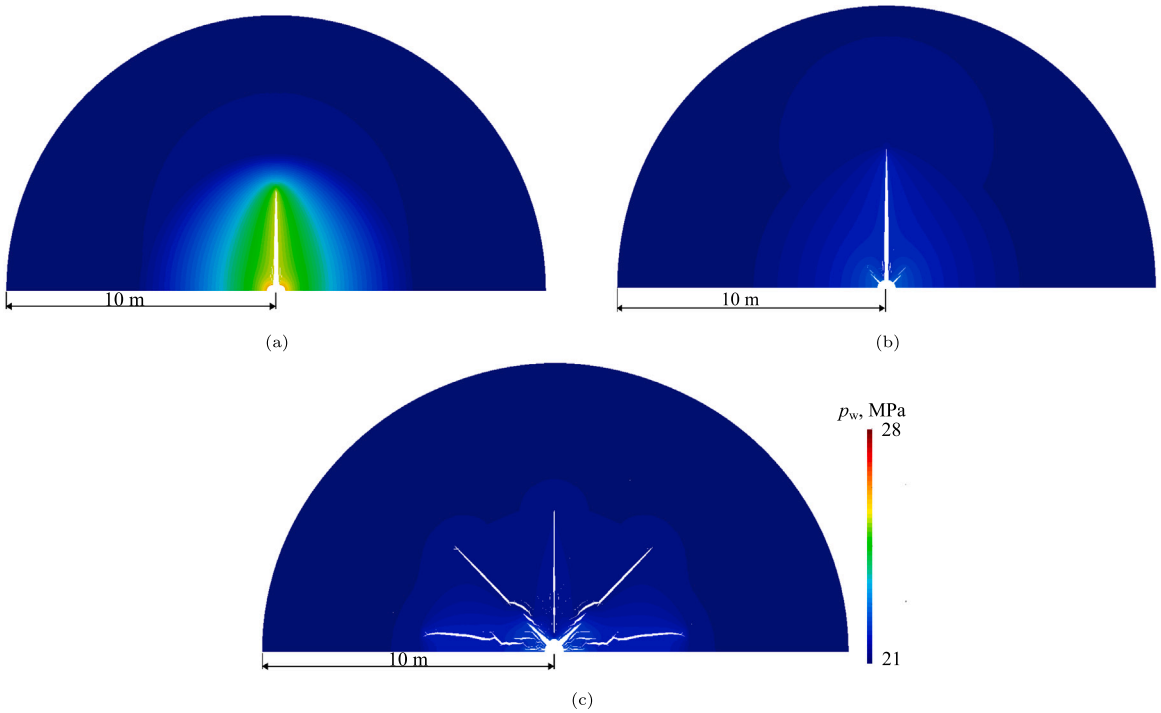

Fig. 13. Pressure distribution at t = 120 h with deformed mesh under different temperature difference (Q_{inj} is fixed at 288 m^3/h) - $M2$ scenario. (a) ΔT = 35 K; (b) ΔT = 40 K; (c) ΔT = 45 K. The deformation is 50 times enlarged, and only the domain within a radius of 10 m is shown.

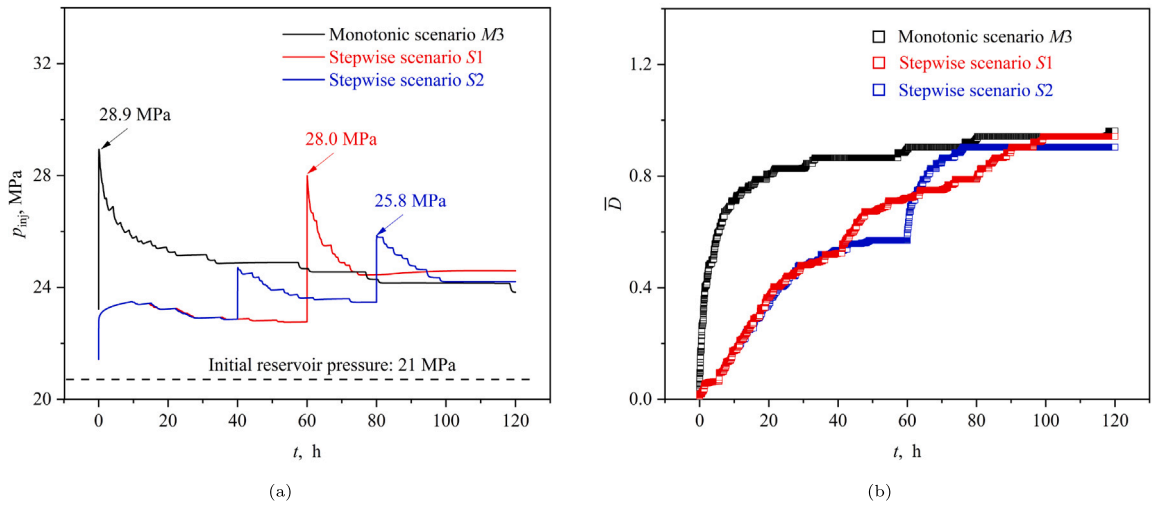

Fig. 14. Comparison of the (a) injection pressure (p_{inj}); and (b) averaged damage variable ($\bar{D}$) evolution under monotonic stimulation scenario $M3$ and stepwise stimulation scenarios $S1$ and $S2$. The temperature difference ΔT is fixed at 40 K.

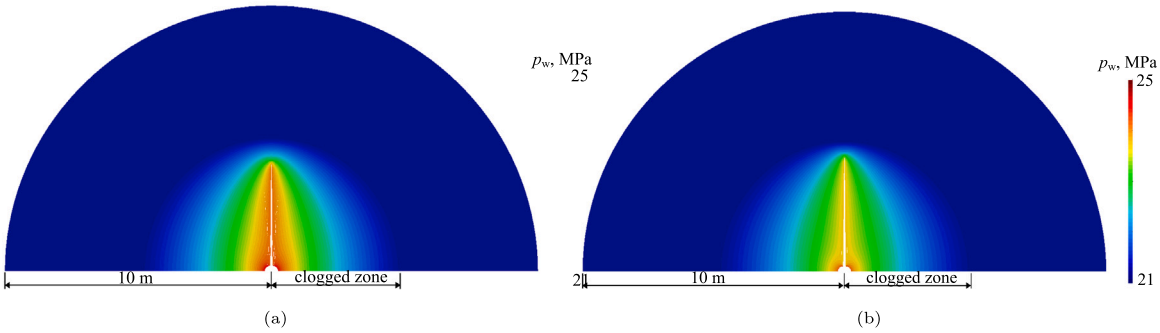

Fig. 15. Pressure distribution of (a) scenario $S1$ and (b) Scenario $S2$ with deformed mesh at t = 120 h (deformation enlarged 100 times), and only the domain within a radius of 10 m is shown.

continuum elements, which results in the early stop of simulations due to lack of convergence (for the case of ΔT = 45 K), as shown in Fig. 11(b). In contrast, ΔT = 35 K does not results in a breakthrough of the clogged zone, with the injection pressure reducing by the least, reducing only to 26 MPa at t = 120 h, with pressure accumulation around the main fracture, shown in Fig. 13(a). In addition, ΔT = 40 K is able to create a breakthrough of the clogged zone, but showing less fracture branching around the borehole (Fig. 13(b)), compared to the case when ΔT = 45 K.

Comparing Figs. 11(a) and 11(b), it demonstrates that both increasing the injection rate Q_{inj} and the temperature difference ΔT can improve the stimulation performance. Yet, increasing the injection rate comes with increasing peak pressure, which could lead to higher risk of inducing seismicity. In contrast, increasing the temperature difference seems to be a more safe and efficient method to improve the simulation performance, with the same peak pressure but significantly more damage and lower injection pressure. However, increasing the temperature difference should be always implemented with care to meet environment regulations and avoid temperature-sensitive clogging processes.

6.2. Reservoir with near-borehole clogging: stepwise stimulation ($S1$–$S2$)

In this section, the stepwise and cyclic stimulation strategies are evaluated, assuming the maximum injection rate Q_{inj}^{max} is 216 m^3/h and the maximum temperature difference ΔT^{max} is 40 K.

Fig. 14 compares the injection pressure (p_{inj}) and averaged damage variable ($\bar{D}$) under monotonic stimulation scenario $M3$ and stepwise stimulation scenario $S1$ and $S2$. It is shown that with stepwise stimulation, compared with monotonic stimulation, a lower maximum injection pressure is achieved with more gradual damage. The three-step scheme ($S2$) leads to better stimulation performance (i.e. a lower maximum injection pressure) than the two-step scheme ($S1$). The highest pressure under monotonic stimulation, shown in Fig. 14(a), is about 28.9 MPa, while that under stepwise stimulation $S1$ is about 27.4 MPa and that under $S2$ is 25.4 MPa, shown in Fig. 14(a). The decreasing maximum injection pressure is because damage is accumulated in the previous steps, in which the injection rate is low.

In the stepwise simulations, the main fracture is shown to be shorter than that under monotonic stimulation, though the main fracture grows to a slightly smaller length in the end of the stimulation (see Fig. 14(b)). At the final time step, the main fracture under scenario $S2$ is longer than that under scenario $S1$, leading to a lower pressure at the borehole and around the main fracture, as shown in Fig. 15. In all scenarios, no high-way connection is made between the borehole and the un-clogged zone, thus relatively high pressure remains around the main fracture — which could be addressed by further increasing the injection rate. Figs. 16(a)–16(d) shows the distribution of the major principal stress evolving with time under the scenario. as an example, $S2$. It shows that the tensile region is controlled by the cooling front propagation. When the injection rate is at 54 m^3/h, the length of the main fracture remains small, as shown in Figs. 16(a) and 16(b). With the stepwise increase in the injection rate to 108 m^3/h and 216 m^3/h, the fracture keeps growing as shown in Figs. 16(c) and 16(d).

It can be concluded that the stepwise stimulation strategy has better stimulation performance than monotonic stimulation, as it reduces

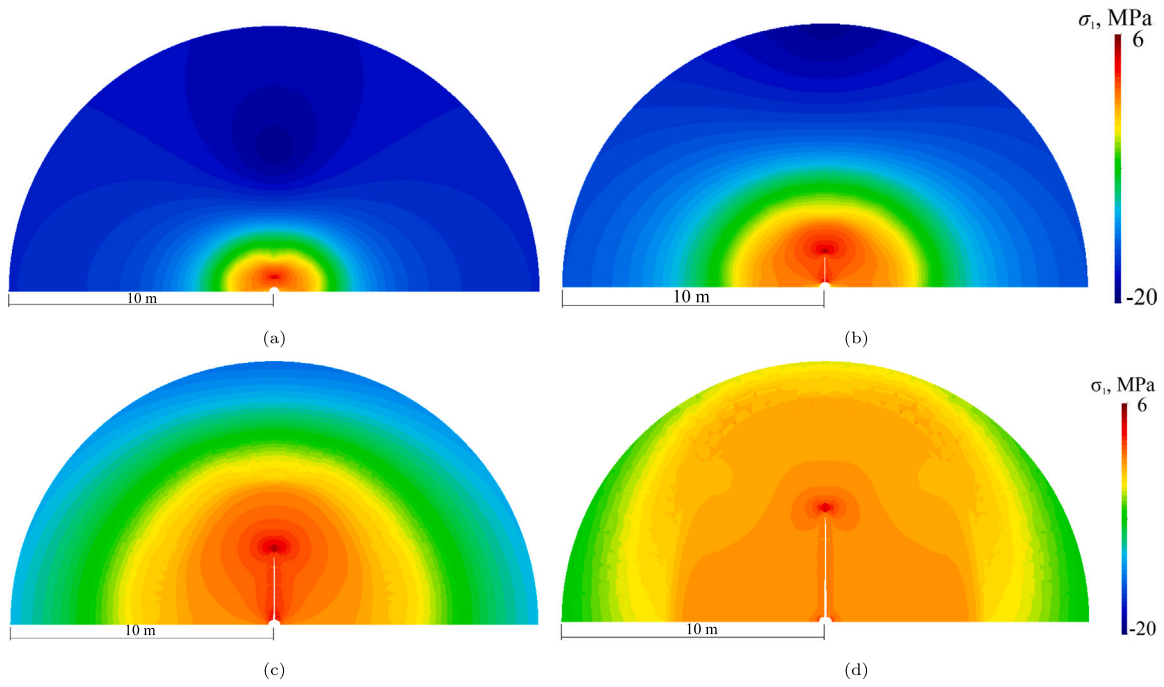

Fig. 16. Distribution of the major principal stress σ_1 at different time steps with deformed mesh under scenario $S2$. (a) t = 10 h; (b) t = 40 h; (c) t = 80 h; (d) t = 120 h. The deformation is 50 times enlarged, and only the domain within a radius of 10 m is shown.

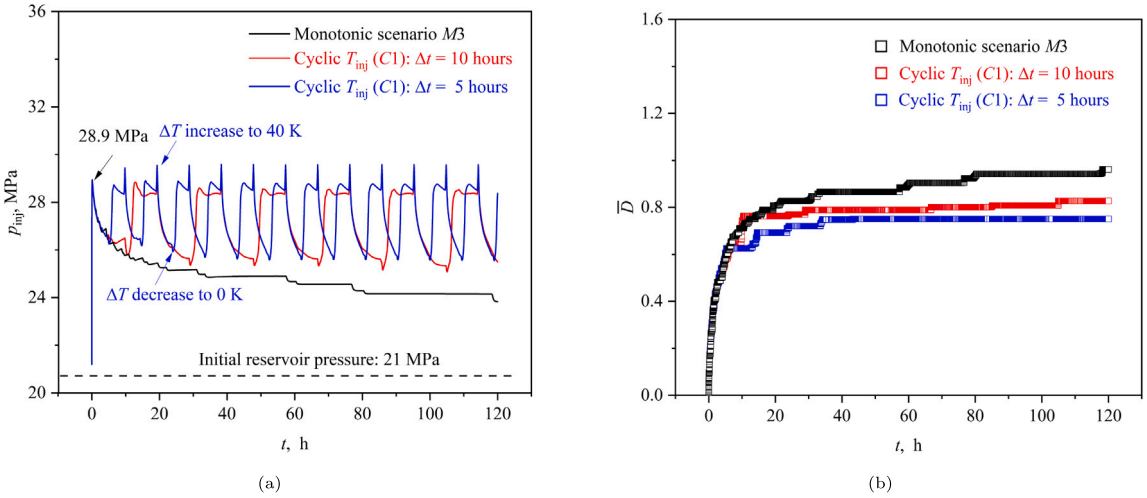

Fig. 17. (a) Injection pressure evolution; and (b) corresponding averaged damage variable evolution under monotonic and cyclic-temperature stimulation with Q_{inj} = 216 m^3/h - scenario $C1$. Cyclic period is 5 h and 10 h.

the required peak injection pressure (substantially), reduces long-term injection pressures (slightly) and slightly decreases overall reservoir damage (see Fig. 16).

6.3. Reservoir with near-borehole clogging: cyclic stimulation ($C1$–$C3$)

6.3.1. Scenario $C1$: Cyclic injection temperature

Fig. 17(a) compares the injection pressure response under constant and cyclic-temperature injection. It can be seen that the highest injection pressure during cyclic-temperature injection is slightly higher than that under monotonic stimulation. In addition, the main fracture does not breakthrough the clogged zone in either scenario, as is indicated in Fig. 17(b). In Fig. 18, the main fracture and the fracture branching are longer and larger under monotonic stimulation (the results of pressure are shown in Fig. 12(b), which highlight the fracture extend better) than those under cyclic-temperature stimulation. Yet, there are more secondary fractures induced during cyclic-temperature stimulation. For monotonic stimulation, 6 visible fracture branches can be seen around the borehole/main fracture (Fig. 18(a)), while for cyclic temperature stimulation, 14 fracture branches are induced (Figs. 18(b) and 18(c)).

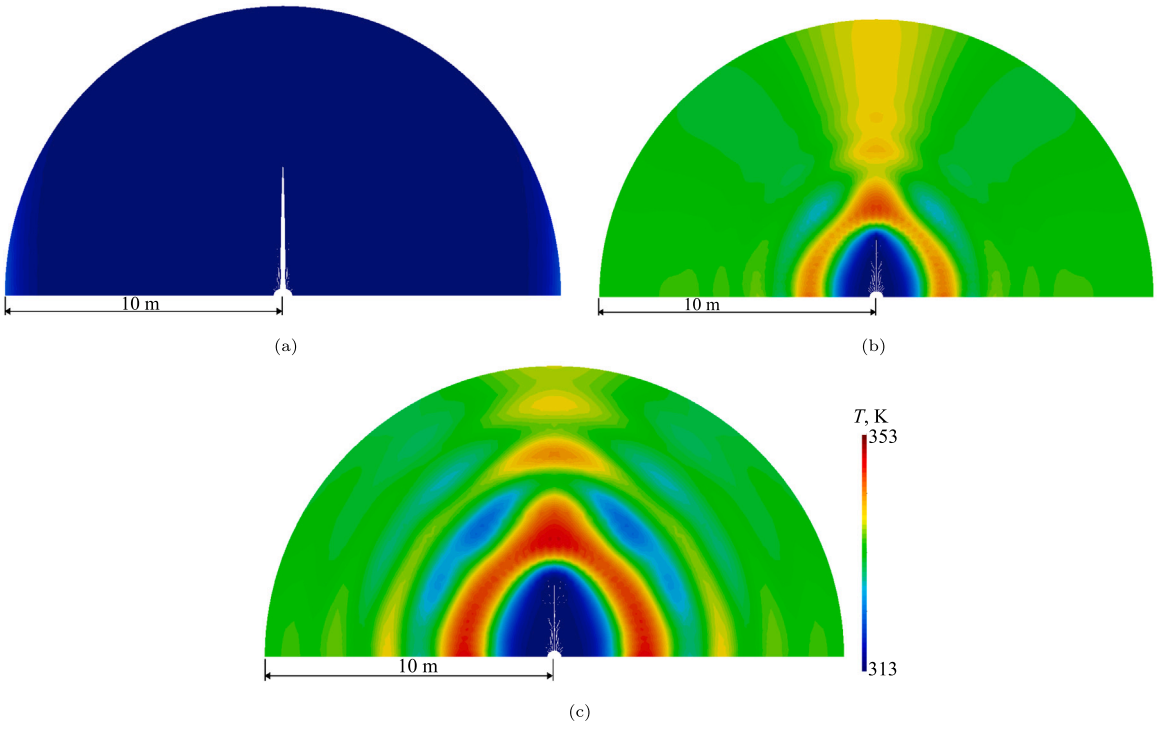

Fig. 18. Temperature distribution at t = 120 h with deformed mesh under (a) monotonic (Q_{inj}^{max} = 216 m^3/h), (b) 5-hour and (c) 10-hour cyclic-temperature stimulation (ΔT = 40 K ↔ 0 K) - scenario $C1$. The deformation is 100 times enlarged.

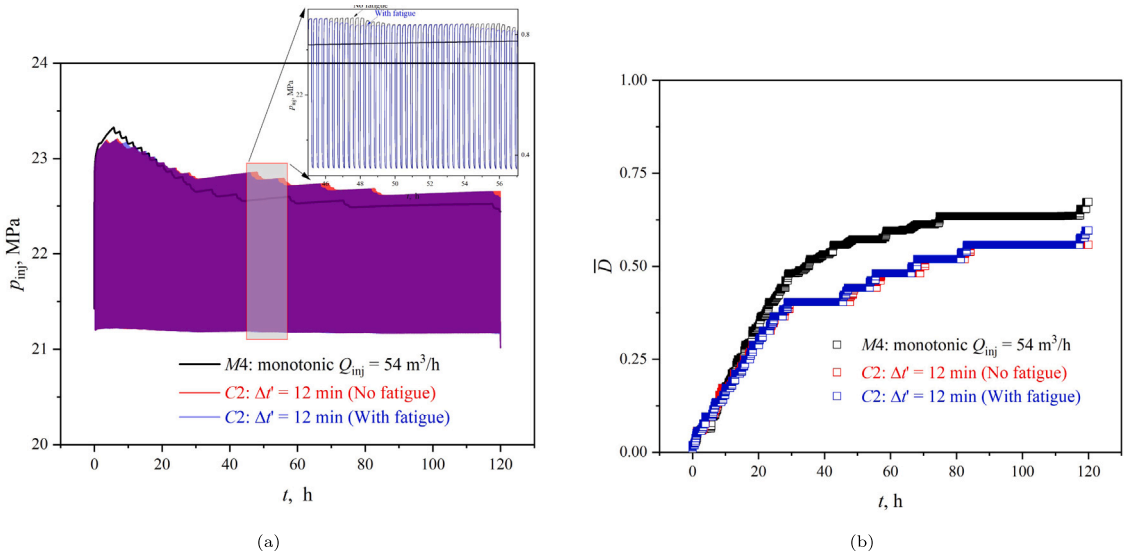

Fig. 19. (a) Injection pressure response and (b) averaged damage variable evolution for scenario $C2$ under 12-min cyclic stimulation (Q_{inj} = 54 m^3/h) with and without fatigue damage variable included in the traction–separation law.

However, the resulting long-term injection pressure is similar in all cases. The extent of the secondary fractures are seen to be controlled by the time period of the injection of cold water, as is shown in Fig. 18. To validate the occurrence of more local damages during field monotonic and cyclic temperature stimulation, micro-seismic monitoring technology, such as distributed acoustic sensing, can be used to monitor and locate the local damages.

It is therefore concluded that cyclic-temperature stimulation (within the bounds of the scenarios considered here) is generally neither better or worse than monotonic stimulation, but has slightly different characteristics. Constant injection creates a larger single fracture which breaks through the clogged zone, whereas thermal cycles create more local damage controlled by the period of the cyclic injection.

6.3.2. *Scenario C2 & C3: Cyclic injection rate*

In Scenario $C2$, cyclic stimulation with a lower maximum injection rate (54 m^3/h) is investigated. Fig. 19(a) compares the pressure response and averaged damage variable under monotonic stimulation $M4$

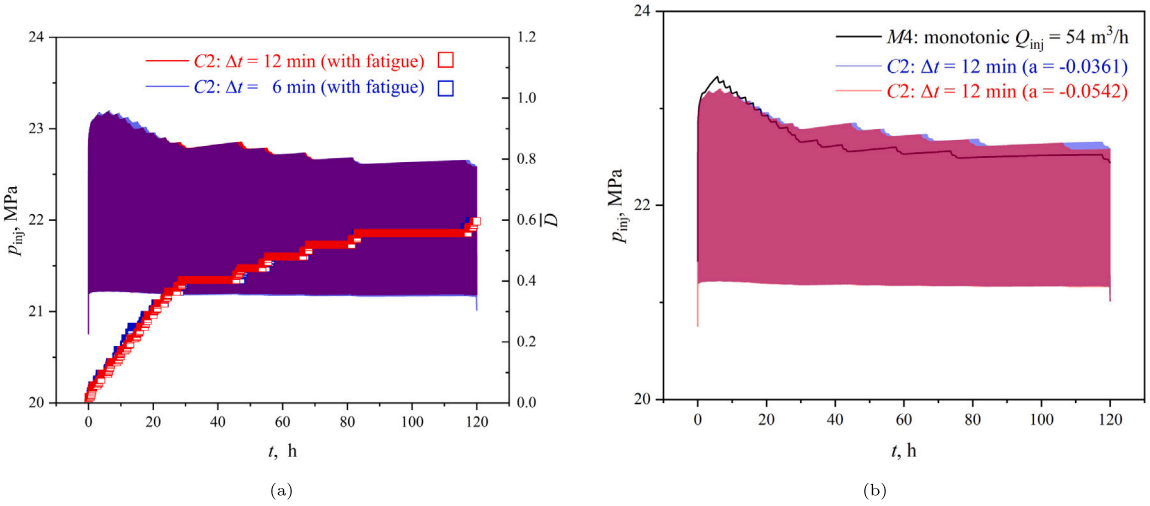

Fig. 20. Comparison of injection pressure response for scenario C2 under (a) different frequency (6 min and 12 min); (b) different S-N curve (a = −0.0361 or −0.0180).

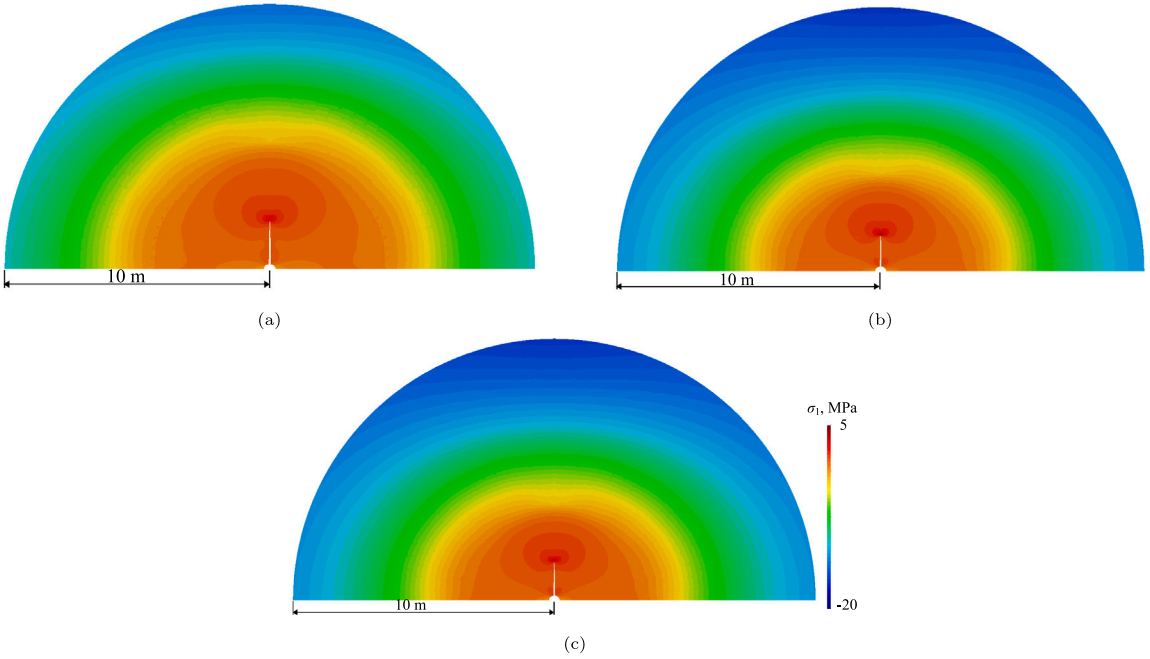

Fig. 21. Horizontal stress (σ_x) distribution at t = 120 h with deformed mesh under (a) monotonic stimulation (scenario $M4$); (b) cyclic stimulation without fatigue damage (scenario $C2$); (c) cyclic stimulation with fatigue damage (scenario $C2$). The deformation is 100 times enlarged, and only the domain within a radius of 10 m is shown.

and 12 min cyclic stimulation with and without the fatigue damage. It shows that the peak pressure under monotonic stimulation is slightly higher than cyclic stimulation. This is because the cyclic injection scheme slows down the pressure build up and at the same time, near-borehole damage is accumulated, resulting lower peak pressure. In the 5-day stimulation, the monotonic scheme shows the best stimulation performance, with a lower maximum injection pressure and longer main fracture (indicated by the averaged damage variable) after the first 20 h. In addition, a comparison of the injection pressure under cyclic stimulation with and without fatigue damage included, demonstrates that fatigue damage makes a minor difference, only causing slightly earlier fracture growth, as can be seen in the enlarged part in Fig. 19(a) and the damage evolution in Fig. 19(b).

Moreover, factors that could impact the fatigue effect are also investigated. Fig. 20(a) compares the injection pressure under different frequency (6 min and 12 min). The results shows that even if the cyclic frequency is increased, the fatigue effect makes little difference. The reason is likely that the growing fractures make the pressure difficult to maintain at a level that can induce fatigue damage within a reasonable number of cycles. This can be seen in Figs. 21(a) and 21(c), in which the major principal stress σ_1 at the fracture tip is shown to be around 3 MPa at t = 120 h, smaller than the tensile strength (4.8 MPa) due

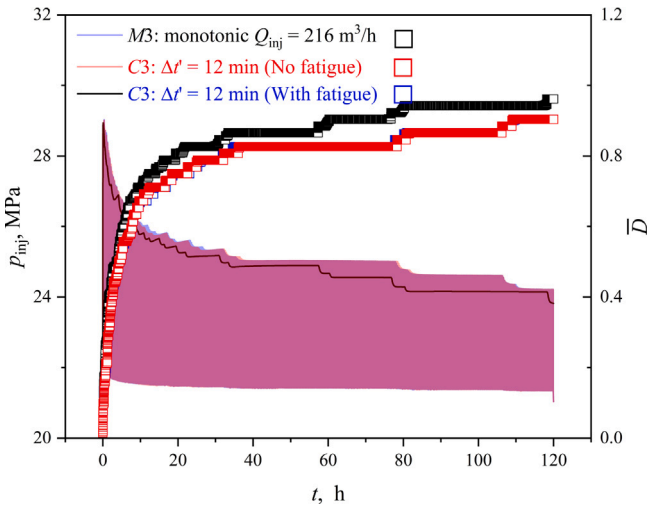

Fig. 22. Injection pressure response and averaged damage variable evolution under 12-min cyclic stimulation (Q_{inj} = 216 m^3/h) with and without fatigue damage variable included in the traction–separation law- scenario $C3$.

to stress relaxation after fracture growth, indicated by the increased averaged damage variable at t = 120 h shown in Fig. 19(a). The continuous increase in the averaged damage variable demonstrates the continuous fracture growth, therefore continuous stress relaxation. In contrast, during the period when the averaged damage variable keeps the constant (i.e. no fracture growth), the fatigue effect still does not make significant difference. This is because the stress applied on the interface element at the fracture tip is too small to induce effective fatigue damage within the cycles before fracture growing. This can be seen for the case of cyclic stimulation without damage variable, shown in Fig. 21(b), the σ_1 at the fracture tip is around 4 MPa, leading to the ratio σ_A/σ_{n0} (i.e. 4/4.8) equal to 83%, which leads to a fatigue life of around 30 000 cycles (see Fig. 6). Consequently, significant fatigue damage cannot be achieved with the current cyclic scheme. In addition, the fitted S-N curve can also make a difference. The parameter a is perturbed to evaluate the impact of the S-N curve. As is shown in Fig. 6, one S-N curve is fitted based on all the collected experimental data, leading to the $a = -0.0361$, while another S-N curve is taken such that $a = -0.0542$ and the fitted curve almost is the lowest envelop of the scattered experimental data. Fig. 20(b) shows the injection pressure response under different assumptions of the S-N curve. A higher slope leads to faster failure, i.e. less cycles. And the result shows this trend in Fig. 20(b), in which the injection pressure reduces earlier in the case of $a = -0.0542$ than that in the case of $a = -0.0361$.

In scenario $C3$, cyclic stimulation with higher maximum injection rate (216 m^3/h) is investigated. Fig. 22 compares the pressure response and averaged damage variable under monotonic stimulation $M3$ and cyclic stimulation $C3$ with and without fatigue damage variable included. It shows the injection pressure under cyclic stimulation is always slightly higher than the monotonic stimulation, except for the initial stage where the cyclic stimulation outperforms the monotonic stimulation, as also observed in scenario $C2$. This is because the higher injection rate leads to quick fracture growth, while cyclic reduction in injection rate slows down the fracture growth. In addition, the underlying mechanism why the fatigue damage does not make a difference is the same with that explained earlier, therefore not repeated here.

6.4. Reservoir with near-borehole clogging: combined cyclic and stepwise stimulation ($CS1$–$CS2$)

In scenarios $CS1$ and $CS2$, the combined cyclic and stepwise stimulation strategy is investigated. Fig. 23(a) compares the pressure response under monotonic stimulation and stimulation scenarios $CS1$ and $CS2$. It shows that the highest spike under monotonic stimulation (28.9 MPa) is significantly reduced to 28 MPa and 25.8 MPa by changing the stimulation scenario to $CS1$ and $CS2$ respectively. Yet, the highest spike is higher than that under only stepwise stimulations, especially the three-step stimulation $S2$. This is because the continuous injection in each step causes longer fracture (as can be seen in Fig. 23(b)) at the end of each step. When the injection rate is increased, the longer fracture leads to lower peak pressure than that under $CS1$ and $CS2$ scenarios. In addition, at t = 80 h–120 h, the injection pressure under $S1$ and $S2$ is significantly lower than that under $CS1$ and $CS2$ respectively. It therefore can be concluded that stepwise combined with cyclic stimulation is better than monotonic stimulation, but is inferior than only stepwise stimulation.

In terms of the total energy input, Fig. 24 compares the total mechanical (pumping) energy input under different stimulation scenarios. The energy is quantified by considering the pumping energy only, assuming that changes in temperature can be achieved by using extracted water mixed with water at ambient temperature (as the temperatures used neither exceed extracted temperatures nor are lower than ambient). The mechanical losses in the wells are ignored, since the wells are designed for higher flow rate than used in the stimulation, thus losses are small.

It show that cyclic injection temperature stimulation leads to the highest total energy input after 120-hour operation, followed by monotonic stimulation scenario $C3$, with a 0.08 TJ difference. This is attributed to the increases in viscosity when decreasing the temperature which result in a higher required injection pressure (see Fig. 23). The cyclic injection rate protocol has further reductions in energy input, with the stepwise or stepwise combined with cyclic injection rate protocols leading to the least total energy input due to its lower injection rate in the first steps and its alternated injection rate, using around half of the input energy than monotonic injection, leading to a significant cost saving. In context of produced energy (albeit energy production is thermal energy and input energy is likely to be electrical), the amounts used are negligible, with such a system producing in the magnitude of TJs per day (depending on the injection temperature).

7. Conclusion

Thermo-hydro-mechanical (THM) finite element simulations of cold water injection into a reservoir are performed to evaluate the potential for thermo-hydraulic stimulation of clogged reservoirs. Interface elements are inserted between all continuum elements to allow for fracture initiation and propagation. The simulations assume a 2D plane strain condition, therefore do not include 3D effects, such as out-of-plane fracture branching, stress arching, or thermal convection, which could influence details of the fracture propagation patterns and pressure response. In addition, the heat exchange between the wellbore fluid, casing and the formation is not included in this model, and could overestimate the thermally-induced stresses. Yet, considering the relatively high flow rate, which leads to higher heat convection, the overestimation is limited.

For a clogged reservoir, simulations of various stimulation strategies – constant, stepwise, cyclic, and combined stepwise-cyclic injection – reveal that stepwise stimulation consistently provides the most favourable outcomes. It achieves the lowest peak injection pressure (4.4 MPa above the initial reservoir pressure, compared to 7.9 MPa in the monotonic case for Q_{inj} = 216 m^3/h and ΔT = 40 K) and maintains slightly lower long-term injection pressures. In addition, it uses the least input energy to achieve this. Cyclic-temperature stimulation (within the bounds of the scenarios considered here) yields broadly comparable results to monotonic stimulation but with distinct fracture patterns: constant injection promotes the formation of a single dominant fracture through the clogged zone, whereas thermal cycles induce more distributed damage controlled by the thermal cycle period. However, due

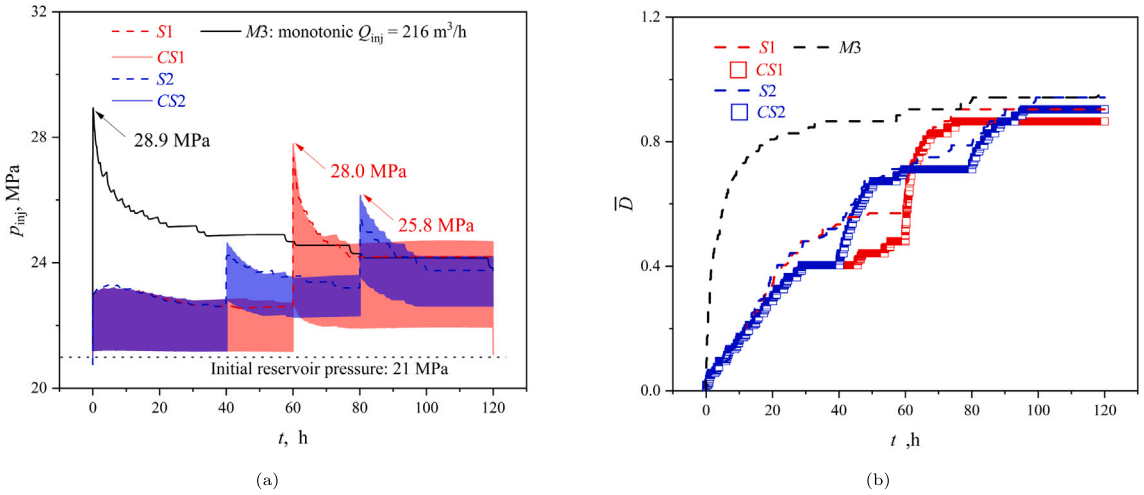

Fig. 23. (a) Injection pressure response under combined cyclic and stepwise stimulation (Scenario $CS1$ and $CS2$); and (b) Corresponding averaged damage variable $\bar{D}$.

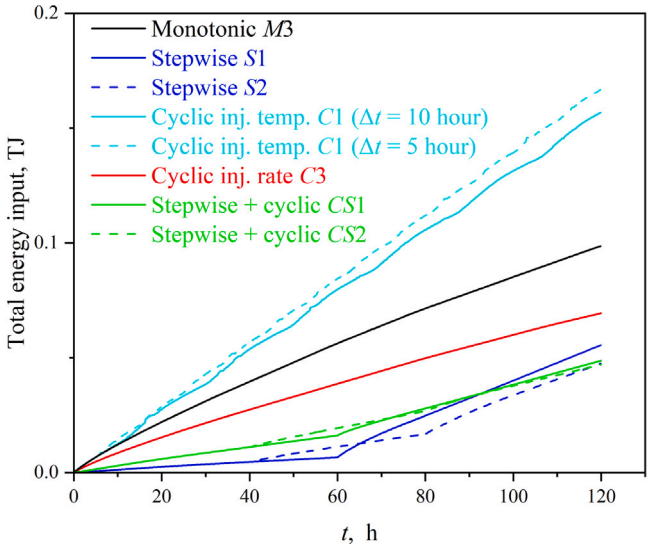

Fig. 24. Total energy input under different stimulation scenarios, including monotonic stimulation ($M3$), Stepwise stimulation $S1$ and $S2$, cyclic injection temperature stimulation $C1$ (with Δt = 10 h or 5 h), cyclic injection rate stimulation $C3$, as well as stepwise combined with cyclic injection rate stimulation $CS1$ and $CS2$.

to the lower visocity of injected cooler water uses the most input energy. Cyclic-injection-rate stimulation exhibits marginal improvement or degradation relative to monotonic stimulation, depending on the injection rate, with fatigue effects remaining negligible. A combined stepwise-cyclic strategy may enhance stimulation performance compared to monotonic stimulation, and consumes least pumping energy than stepwise stimulation alone under the investigated conditions. Although the enhanced permeability may decrease after stimulation with the stress recovery, continuous reinjection of cold water, as a necessary operation in geothermal projects, can relieve this impact.

CRediT authorship contribution statement

Wen Luo: Writing – review & editing, Writing – original draft, Visualization, Validation, Software, Methodology, Investigation, Formal analysis, Data curation, Conceptualization. **Anne-Catherine Dieudonné:** Writing – review & editing, Supervision, Software, Methodology, Formal analysis, Conceptualization. **Josselin Ouf:** Writing – review & editing, Software, Formal analysis. **Philip J. Vardon:** Writing – review & editing, Validation, Supervision, Project administration, Methodology, Funding acquisition, Formal analysis, Conceptualization.

Declaration of competing interest

The authors declare that they have no known competing financial interests or personal relationships that could have appeared to influence the work reported in this paper

Acknowledgements

This project has received funding from the European Union's Horizon 2020 research and innovation programme under the Marie Skłodowska-Curie grant agreement No 956965. Support and help from Joaquín Liaudat throughout this research is gratefully acknowledged.

Appendix. Method to reduce hydraulic and thermal artificial compliance

The placement of interface elements between continuum elements has been shown not to affect the stress, pressure or temperature fields of intact rock when parameters are appropriately chosen. In particular, the stiffness of the interface elements should be set high enough to reduce the mechanical artificial compliance without causing numerical instability. Similarly, to properly address the thermal and hydraulic artificial conductivity, the transversal hydraulic transmissivity should be set as high as possible to minimise the pressure and temperature drops across the interface elements.

However, a high transversal hydraulic transmissivity can result in fast heat convection accross the interface elements. It is well known that fast heat convection in comparison to conduction can lead to numerical oscillation. The Péclet number, a dimensionless number that quantifies the relative importance of convective heat transport compared to conductive heat transport, is used to characterise the dominant heat transfer mechanism. It is defined as:

$$Pe = \frac{\rho_w c_{pw} h v_w^{b/t}}{2\lambda_w} \quad \text{(transversal)} \tag{A.1}$$

where ρ_w [m³/h], c_{pw} [J/kg K] and λ_w [W/m K] are the water density, specific heat capacity and heat conductivity respectively. $v_w^{b/t}$ [m/s] is

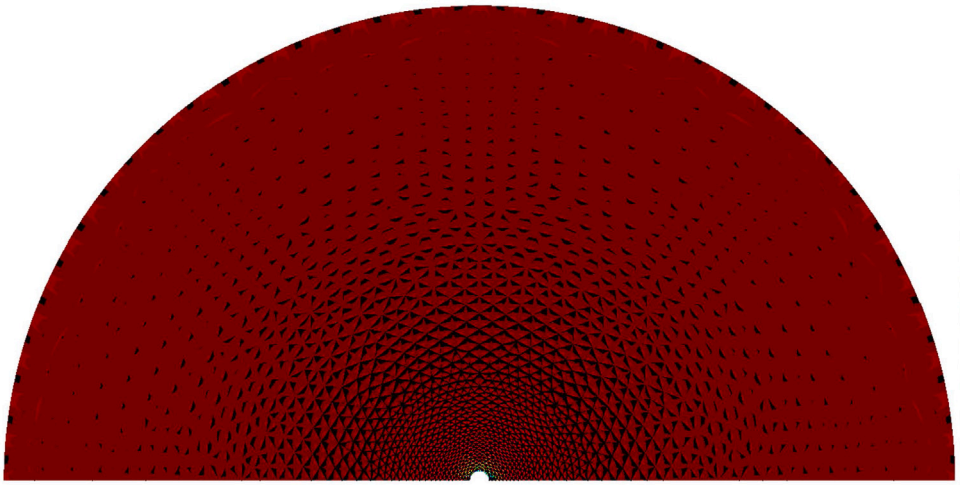

(a) Temperature field without stabilisation. t = 30 s

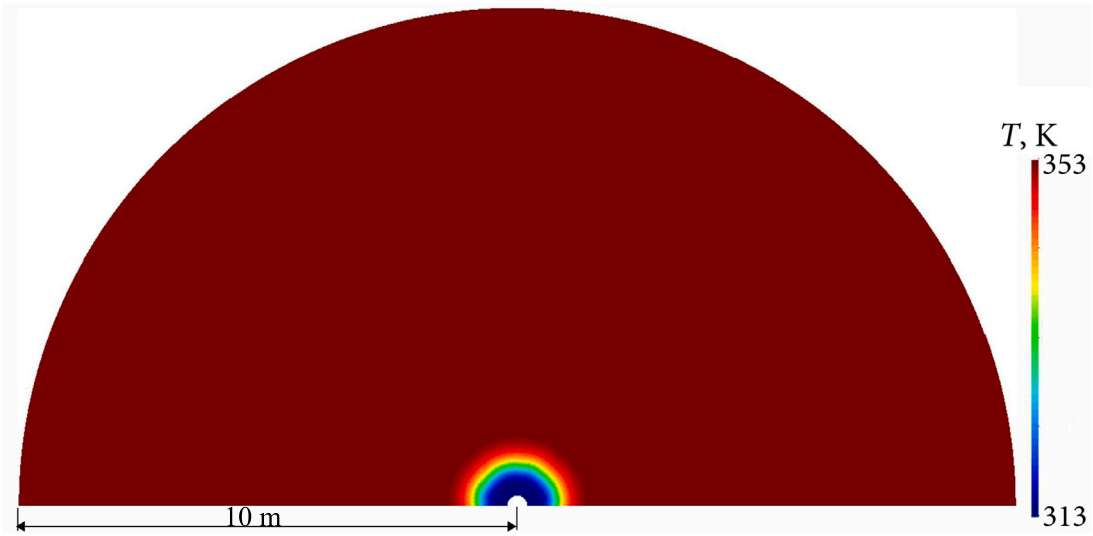

(b) Temperature field with stabilisation ($\delta \times h = 10$). t = 2000 s

Fig. A.1. Comparison of temperature fields (model region within radius of 10 m is shown here) with and without stabilisation technique for high Péclet number. The simulation without stabilisation is stopped at $t = 30$ s due to numerical divergence and temperature solution is with numerical oscillation. The black spots indicate values outside the legend range 313 K–353 K. In contrast, the simulation with stabilisation can run smoothly without oscillation.

the transversal fluid velocity (from bottom or top side of the interface element). h [m] is the element length.

A high Péclet corresponds to a convection-dominated transfer mechanism. In Luo et al. [26], it is shown that high longitudinal heat convection within the interface elements can result in numerical oscillation, and that adding an artificial conductivity can stabilise the solution. In the present case, transversal heat convection will also be high due to the imposed high transversal transmissivity. Therefore, in this section, an artificial conductivity is added to the transversal heat transfer terms. It is expressed as:

$$\lambda_a = \delta \rho_w c_{pw} h \left| v_w^{b/t} \right| \quad \text{(transversal)} \tag{A.2}$$

where δ is a tuning parameter. Consequently, the Péclet number with stabilisation reads:

$$Pe = \frac{\rho_w c_{pw} h v_w^{b/t}}{2(\lambda_a + \lambda_w)} \quad \text{(transversal)} \tag{A.3}$$

To demonstrate the stabilisation technique, thermo-hydraulic (T-H) simulations of the injection of cold water using the model equipped with interface elements with and without stabilisation are first compared. Then, T-H simulations using the model with interface elements and the model without interface elements are compared to demonstrate the capability of the modelling approach (i.e. increasing the transversal hydraulic conductivity of the interface element with stabilised technique) to reproduce the thermal and hydraulic fields of the intact rock. The parameters of the continuum and interface elements as well as boundary and initial conditions are the same as is presented earlier in Tables 1 and 2. The injection rate Q_{inj} is assumed to be 72 m^3/h with injection temperature at 313 K.

Fig. A.1 compares temperature fields calculated without and with stabilisation technique, of simulations on the domain including interface elements. Significant oscillation is seen to occur if no stabilisation technique is used, and the simulation stops at $t = 30$ s due to lack of numerical convergence. In contrast, when the stabilisation technique is used (with $\delta \times h = 10$ m), the simulation is seen to run smoothly and continuously without any numerical oscillation.

The second set of simulations investigates whether the model equipped with interface elements, utilising high transversal transmissivity and stabilisation, can reproduce the hydraulic and thermal fields of intact rock. To investigate this, two model domains are used and the results compared. The first model only consists of continuum elements,

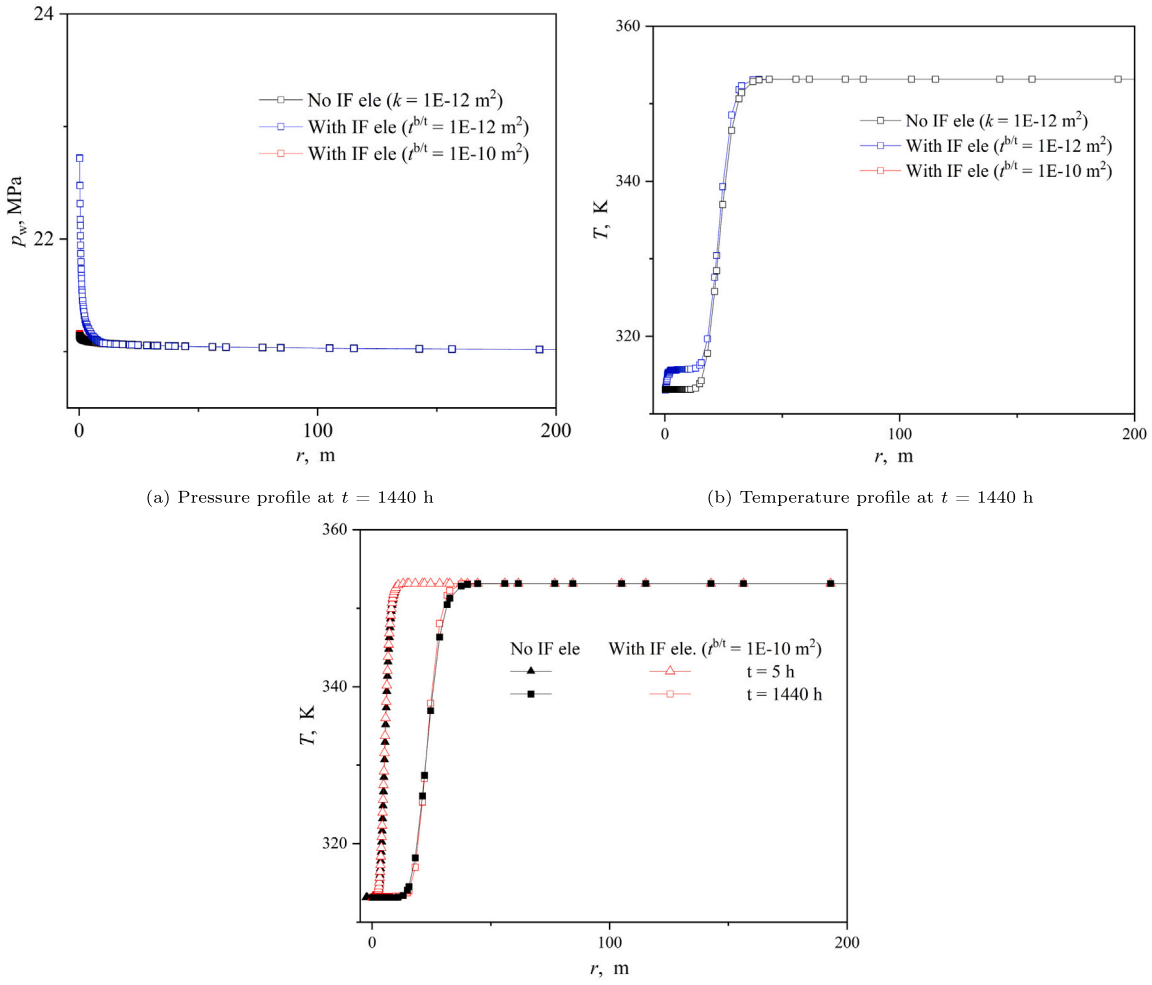

(a) Pressure profile at t = 1440 h

(b) Temperature profile at t = 1440 h

(c) Temperature profile after 5 and 1440 hours of cold water injection

Fig. A.2. Comparison of (a) pressure (t = 1440 h) and (b) temperature (t = 1440 h) distributions with and without interface elements inserted in between all the continuum elements in the region with a radius of 10 m. When the transversal hydraulic conductivity is 1E−10 m^2 respectively, the pressure and temperature distribution can be reproduced. (c) Comparison of temperature distribution evolving with time, of the model equipped with interface element ($t^{b/t}$ = 1E−10 m^2) and without interface element.

representing intact rock, while the other is composed of continuum elements and interface elements. Two variants of the model with interface elements are used to investigate the impact of the transversal hydraulic transmissivity. As before, thermo-hydraulic simulations with same boundary and initial conditions are performed. Figs. A.2(a) and A.2(b) compare the spatial distribution of pressure and temperature of all three results. Fig. A.2(c) presents the temperature results for an additional time step of the intact and most successful stabilised solution. The results show that when the transversal hydraulic transmissivity of the interface elements is 1E−10 m^2, the temperature and pressure distributions are imperceptibly different from those of the model without interface elements. In contrast, when the transversal hydraulic transmissivity is 1E−12 m^2, there is a large difference in the zone with the interface elements. The comparison confirms that the values of transversal fluid/heat transmissivity must be carefully selected, in order to have realistic results, but this may require the use of a stabilisation technique to address the resulting numerical oscillation due to high Péclet number.

Data availability

Data will be made available on request.

References

[1] Mignan A, Landtwing D, Kästli P, Mena B, Wiemer S. Induced seismicity risk analysis of the 2006 Basel, Switzerland, Enhanced Geothermal System project: Influence of uncertainties on risk mitigation. Geothermics 2015;53:133–46. http://dx.doi.org/10.1016/j.geothermics.2014.05.007.

[2] Kim K-I, Yoo H, Park S, Yim J, Xie L, Min K-B, Rutqvist J. Induced and triggered seismicity by immediate stress transfer and delayed fluid migration in a fractured geothermal reservoir at Pohang, South Korea. Int J Rock Mech Min Sci 2022;153:105098. http://dx.doi.org/10.1016/j.ijrmms.2022.105098.

[3] Lengliné O, Schmittbuhl J, Drif K, Lambotte S, Grunberg M, Kinscher J, Sira C, Schlupp A, Schaming M, Jund H, et al. The largest induced earthquakes during the GEOVEN deep geothermal project, Strasbourg, 2018–2022: from source parameters to intensity maps. Geophys J Int 2023;234(3):2445–57. http://dx.doi.org/10.1093/gji/ggad255.

[4] Hofmann H, Zimmermann G, Farkas M, Huenges E, Zang A, Leonhardt M, Kwiatek G, Martinez-Garzon P, Bohnhoff M, Min K-B, Fokker P, Westaway R, Bethmann F, Meier P, Yoon KS, Choi JW, Lee TJ, Kim KY. First field application of cyclic soft stimulation at the Pohang Enhanced Geothermal System site in Korea. Geophys J Int 2019;217(2):926–49. http://dx.doi.org/10.1093/gji/ggz058.

[5] Luviano MS, Flores Armenta M, Montes MR. Thermal stimulation to improve the permeability of geothermal wells in Los Humeros geothermal field, Mexico. In: World geothermal congress 2015. Melbourne, Australia; 2015, URL https://www.worldgeothermal.org/pdf/IGAstandard/WGC/2015//22017.pdf.

[6] Zhuang L, Kim KY, Jung SG, Diaz M, Min KB, Zang A, Stephansson O, Zimmermann G, Yoon JS, Hofmann H. Cyclic hydraulic fracturing of pocheon

granite cores and its impact on breakdown pressure, acoustic emission amplitudes and injectivity. Int J Rock Mech Min Sci 2019;122:104065. http://dx.doi.org/10.1016/j.ijrmms.2019.104065.
[7] Zimmermann G, Moeck I, Blöcher G. Cyclic waterfrac stimulation to develop an enhanced geothermal system (EGS)—conceptual design and experimental results. Geothermics 2010;39(1):59–69. http://dx.doi.org/10.1016/j.geothermics.2009.10.003.
[8] Gunnarsson G. Mastering reinjection in the Hellisheiði field, SW-Iceland: A story of successes and failures. In: 36th workshop on geothermal reservoir gngineering. Stanford, Canifornia: Stanford University; 2011, URL https://es.stanford.edu/ERE/pdf/IGAstandard/SGW/2011/gunnarsson1.pdf.
[9] Zimmerman RW. Coupling in poroelasticity and thermoelasticity. Int J Rock Mech Min Sci 2000;37(1–2):79–87. http://dx.doi.org/10.1016/S1365-1609(99)00094-5.
[10] De Simone S, Vilarrasa V, Carrera J, Alcolea A, Meier P. Thermal coupling may control mechanical stability of geothermal reservoirs during cold water injection. Phys Chem Earth 2013;64:117–26. http://dx.doi.org/10.1016/j.pce.2013.01.001.
[11] Veldkamp JG, Loeve D, Peters E, Nair R, Pizzocolo F, Wilschut F. Thermal fracturing due to low injection temperatures in geothermal doublets. Technical Report R11739, Utrecht: TNO; 2016, p. 7–9, URL https://publications.tno.nl/publication/34620511/yg2gxI/TNO-2015-R11739.pdf.
[12] Terzaghi K. Theoretical Soil Mechanics. John Wiley & Sons, Inc.; 1943, http://dx.doi.org/10.1002/9780470172766, URL https://onlinelibrary.wiley.com/doi/book/10.1002/9780470172766.
[13] Zang A, Zimmermann G, Hofmann H, Niemz P, Kim KY, Diaz M, Zhuang L, Yoon JS. Relaxation damage control via fatigue-hydraulic fracturing in granitic rock as inferred from laboratory-, mine-, and field-scale experiments. Sci Rep 2021;11(1):6780. http://dx.doi.org/10.1038/s41598-021-86094-5.
[14] Yoshioka K, Izgec B, Pasikki R. Optimization of geothermal well stimulation design using a geomechanical reservoir simulator. In: The 33th workshop on geothrmal reservoir engineering. Stanford, California; 2008, URL https://earthsci.stanford.edu/ERE/pdf/IGAstandard/SGW/2008/yoshioka.pdf.
[15] Yoon JS, Zang A, Stephansson O. Numerical investigation on optimized stimulation of intact and naturally fractured deep geothermal reservoirs using hydro-mechanical coupled discrete particles joints model. Geothermics 2014;52:165–84. http://dx.doi.org/10.1016/j.geothermics.2014.01.009.
[16] Jacquey AB, Urpi L, Cacace M, Blöcher G, Zimmermann G, Scheck-Wenderoth M. Far field poroelastic response of geothermal reservoirs to hydraulic stimulation treatment: Theory and application at the groß schönebeck geothermal research facility. Int J Rock Mech Min Sci 2018;110:316–27. http://dx.doi.org/10.1016/j.ijrmms.2018.08.012.
[17] Cheng Q, Wang X, Ghassemi A. Numerical simulation of reservoir stimulation with reference to the Newberry EGS. Geothermics 2019;77:327–43. http://dx.doi.org/10.1016/j.geothermics.2018.09.011.
[18] Yoo H, Park S, Xie L, Kim K-I, Min K-B, Rutqvist J, Rinaldi AP. Hydro-mechanical modeling of the first and second hydraulic stimulations in a fractured geothermal reservoir in Pohang, South Korea. Geothermics 2021;89:101982. http://dx.doi.org/10.1016/j.geothermics.2020.101982.
[19] Wang Y, Yuan Y, Guo B, Lei H, Zhu H, Tian H, Xu T. Numerical simulation of hydro-shearing stimulation in the enhanced geothermal system at the Utah FORGE site. Eng Geol 2024;343:107823. http://dx.doi.org/10.1016/j.enggeo.2024.107823.
[20] Zhang Z, Peng S, Ghassemi A, Ge X. Simulation of complex hydraulic fracture generation in reservoir stimulation. J Pet Sci Eng 2016;146:272–85. http://dx.doi.org/10.1016/j.petrol.2016.04.037.
[21] Xi X, Yang S, McDermott CI, Shipton ZK, Fraser-Harris A, Edlmann K. Modelling rock fracture induced by hydraulic pulses. Rock Mech Rock Eng 2021;54(8):3977–94. http://dx.doi.org/10.1007/s00603-021-02477-0.
[22] Wei C, Li S, Yu L, Zhang B, Liu R, Pan D, Zhang F. Study on mchanism of strength deterioration of rock-like specimen and fracture damage deterioration model under pulse hydraulic fracturing. Rock Mech Rock Eng 2023;56(7):4959–73. http://dx.doi.org/10.1007/s00603-023-03313-3.
[23] Charlier R. Approche unifiée de quelques problèmes non linéaires de mécanique des milieux continus par la méthode des éléments finis (grandes déformations des métaux et des sols, contact unilatéral de solides, conduction thermique et écoulements en milieu poreux) (Ph.D. thesis), Liège: University of Liège; 1987, p. 301, URL https://hdl.handle.net/2268/315205.
[24] Collin F, Li X, Radu J, Charlier R. Thermo-hydro-mechanical coupling in clay barriers. Eng Geol 2002;64(2–3):179–93. http://dx.doi.org/10.1016/S0013-7952(01)00124-7.
[25] Liaudat J, Dieudonné AC, Vardon PJ. Modelling gas fracturing in saturated clay samples using triple-node zero-thickness interface elements. Comput Geotech 2023;154:105128. http://dx.doi.org/10.1016/j.compgeo.2022.105128.
[26] Luo W, Liaudat J, Ouf J, Dieudonné A-C, Amann F, Vardon PJ. Numerical modelling of fracturing processes during cold water injection into geothermal reservoirs: Verification and qualitative validation. Comput Geotech 2025;183:107186. http://dx.doi.org/10.1016/j.compgeo.2025.107186.
[27] Luo W. Study of near-borehole thermo-hydro-mechanical processes (Ph.D. thesis), Delft: Delft University of Technology; 2026, URL https://doi.org/10.4233/uuid:75953590-d68d-428a-94b5-1e25a7255677.
[28] Costa A. Permeability-porosity relationship: A reexamination of the Kozeny-Carman equation based on a fractal pore-space geometry assumption. Geophys Res Lett 2006;33(2). http://dx.doi.org/10.1029/2005GL025134.
[29] Ewen J, Thomas HR. Heating unsaturated medium sand. Géotechnique 1989;39(3):455–70. http://dx.doi.org/10.1680/geot.1989.39.3.455.
[30] Jaeger JC, Cook NG, Zimmerman R. Fundamentals of rock mechanics. fourth ed.. Wiley-Blackwell; 2009, p. 197–203.
[31] Zimmerman RW, Yeo I-W. Fluid flow in rock fractures: From the Navier-Stokes equations to the cubic law. In: Dynamics of fluids in fractured rock. Vol. 122, Wiley; 2000, p. 213–24. http://dx.doi.org/10.1029/GM122p0213.
[32] Mi Y, Crisfield MA, Davies GAO, Hellweg HB. Progressive delamination using interface elements. J Compos Mater 1998;32(14):1246–72. http://dx.doi.org/10.1177/002199839803201401.
[33] Cerfontaine B, Dieudonné AC, Radu JP, Collin F, Charlier R. 3D zero-thickness coupled interface finite element: formulation and application. Comput Geotech 2015;69:124–40. http://dx.doi.org/10.1016/j.compgeo.2015.04.016.
[34] Lei Q, Barton N. On the selection of joint constitutive models for geomechanics simulation of fractured rocks. Comput Geotech 2022;145:104707. http://dx.doi.org/10.1016/j.compgeo.2022.104707.
[35] Nojavan S, Schesser D, Yang QD. An in situ fatigue-CZM for unified crack initiation and propagation in composites under cyclic loading. Compos Struct 2016;146:34–49. http://dx.doi.org/10.1016/j.compstruct.2016.02.060.
[36] Chen X, Bu J, Fan X, Lu J, Xu L. Effect of loading frequency and stress level on low cycle fatigue behavior of plain concrete in direct tension. Constr Build Mater 2017;133:367–75. http://dx.doi.org/10.1016/j.conbuildmat.2016.12.085.
[37] Cerfontaine B, Collin F. Cyclic and fatigue behaviour of rock materials: Review, interpretation and research perspectives. Rock Mech Rock Eng 2018;51(2):391–414. http://dx.doi.org/10.1007/s00603-017-1337-5.
[38] Lequesne C. Modeling of fracture in heavy steel welded beam-to-column connection submitted to cyclic loading by finite elements (Ph.D. thesis), Liège: Université de Liège; 2009, URL https://orbi.uliege.be/handle/2268/315091.
[39] Vardon PJ, Abels HA, Barnhoorn A, Daniilidis A, Bruhn D, Drijkoningen G, Elliott K, van Esser B, Laumann S, van Paassen P, Vargas Meleza L, Vondrak AG, Voskov D. A research and energy production geothermal project on the TU Delft campus: project implementation and initial data collection. In: 49th workshop on geothermal reservoir engineering. Stanford, California: Stanford University; 2024, URL https://pangea.stanford.edu/ERE/db/GeoConf/papers/SGW/2024/Vardon.pdf.
[40] Vardon PJ, Laumann SJ, van Esser BTM, Ursem LJH, van Schravendijk B, Vargas Meleza L, Barnhoorn A, Abels HA, Vondrak AG, Drijkoningen GG, van Paassen PAM, Elliott KN, van den Berg JJ, Friebel M. End-of-well science programme report DEL-GT-01 and DEL-GT-02: TU Delft campus geothermal project. Technical Report, Delft: Delft University of Technology; 2024, http://dx.doi.org/10.4233/uuid:6ce07471-6986-434e-aa24-ad6e1f6714d9.
[41] Aramburo Velez DA. Synergy between geothermal and stranded oil fields to add value to geothermal projects Master's thesis, Delft University of Technology; 2017, p. 27–8, URL https://www.ebn.nl/wp-content/uploads/2017/11/Aramburo_D._Synergy_between_geothermal_and_stranded_oil_fields_to_add_value_to_geothermal_projects.pdf.
[42] Soustelle V, ter Heege J, Buijze L, Wassing B. Thermomechanical parameters of geothermal analogue reservoir sandstone in the West Netherlands Basin. Technical Report, Utrecht: TNO; 2022, URL https://www.warmingup.info/documenten/thermomechanical-parameters-of-geothermal.pdf.
[43] Voskov D, Abels H, Barnhoorn A, Chen Y, Daniilidis A, Bruhn D, Drijkoningen G, Geiger S, Laumann S, Song G, Vardon PJ, Vargas Meleza L, Verschuur E, Vondrak A. A research and production geothermal project on the TU Delft campus: initial modeling and establishment of a digital twin. In: 49th workshop on geothermal reservoir engineering. California: Stanford University; 2024, URL https://pangea.stanford.edu/ERE/db/GeoConf/papers/SGW/2024/Voskov.pdf.
[44] Baisch S, Vörös R, Rothert E, Stang H, Jung R, Schellschmidt R. A numerical model for fluid injection induced seismicity at Soultz-sous-Forêts. Int J Rock Mech Min Sci 2010;47(3):405–13.
[45] Park S, Xie L, Kim K-I, Kwon S, Min K-B, Choi J, Yoon W-S, Song Y. First hydraulic stimulation in fractured geothermal reservoir in Pohang PX-2 well. Procedia Eng 2017;191:829–37. http://dx.doi.org/10.1016/j.proeng.2017.05.250.